The Astrophysical Journal, 745:92 (17pp), 2012 January 20 doi:10.1088/0004-637X/745/1/92

THE CENTRAL DARK MATTER DISTRIBUTION OF NGC 2976*

Joshua J. Adams[1,2], Karl Gebhardt[1,3], Guillermo A. Blanc[1,2], Maximilian H. Fabricius[4], Gary J. Hill[3,5], Jeremy D. Murphy[1], Remco C. E. van den Bosch[5,6], and Glenn van de Ven[6]

[1] Department of Astronomy, University of Texas at Austin, 1 University Station C1400, Austin, TX 78712, USA
[2] Observatories of the Carnegie Institution of Washington, 813 Santa Barbara Street, Pasadena, CA 91101, USA
[3] Texas Cosmology Center, University of Texas at Austin, 1 University Station C1400, Austin, TX 78712, USA
[4] Max-Planck Institut für extraterrestrische Physik, Giessenbachstrasse, D-85741 Garching bei München, Germany
[5] McDonald Observatory, University of Texas at Austin, 1 University Station C1402, Austin, TX 78712, USA
[6] Max-Planck Institut für Astronomie, Königstuhl 17, 69117 Heidelberg, Germany
Received 2011 July 22; accepted 2011 October 26; published 2012 January 3

ABSTRACT

We study the mass distribution in the late-type dwarf galaxy NGC 2976 through stellar kinematics obtained with the Visible Integral Field Replicable Unit Spectrograph Prototype and anisotropic Jeans models as a test of cosmological simulations and baryonic processes that putatively alter small-scale structure. Previous measurements of the Hα emission-line kinematics have determined that the dark matter halo of NGC 2976 is most consistent with a cored density profile. We find that the stellar kinematics are best fit with a cuspy halo. Cored dark matter halo fits are only consistent with the stellar kinematics if the stellar mass-to-light ratio is significantly larger than that derived from stellar population synthesis, while the best-fitting cuspy model has no such conflict. The inferred mass distribution from a harmonic decomposition of the gaseous kinematics is inconsistent with that of the stellar kinematics. This difference is likely due to the gas disk not meeting the assumptions that underlie the analysis such as no pressure support, a constant kinematic axis, and planar orbits. By relaxing some of these assumptions, in particular the form of the kinematic axis with radius, the gas-derived solution can be made consistent with the stellar kinematic models. A strong kinematic twist in the gas of NGC 2976's center suggests caution, and we advance the mass model based on the stellar kinematics as more reliable. The analysis of this first galaxy shows promising evidence that dark matter halos in late-type dwarfs may in fact be more consistent with cuspy dark matter distributions than earlier work has claimed.

Key words: dark matter – galaxies: dwarf – galaxies: individual (NGC 2976) – galaxies: kinematics and dynamics – galaxies: spiral

Online-only material: color figures

1. INTRODUCTION

The observations of kinematics in low surface brightness (LSB) and dwarf-late-type galaxies have stubbornly resisted giving clear evidence for the cuspy Navarro–Frenk–White (NFW) dark matter (DM) halo profiles that *N*-body simulations with ΛCDM inputs predict (Navarro et al. 1996b). Instead, most LSBs and late-type dwarfs suggest cored DM halos (e.g., Oh et al. 2008, 2011; de Blok et al. 2008; Kuzio de Naray et al. 2008; Spano et al. 2008) or the observations are not constraining enough to rule out cusps (Swaters et al. 2003; Rhee et al. 2004; Simon et al. 2005; Valenzuela et al. 2007). Some simulations have produced cored DM halos by rapidly removing the baryonic disk, which causes the DM halo to expand to a cored equilibrium (Navarro et al. 1996a), initializing numerical simulations with a primordial bar that forms a resonance with and disrupts the cusp (Weinberg & Katz 2002), or by implementing a supernova feedback recipe in high-resolution hydrodynamical simulations (Governato et al. 2010). This puzzle has also motivated proposals for additional particle properties of DM beyond the weakly interacting, cold paradigm such as collisional DM (e.g., Spergel & Steinhardt 2000), warm DM (e.g., Hogan & Dalcanton 2000), and ultra-light boson fluid models (e.g., Peebles 2000; Goodman 2000; Rindler-Daller & Shapiro 2011). Other questions critically rely on knowing the DM density structure in galaxies, such as the prospects of DM annihilation searches that depend sensitively on the true density profile in galaxies (e.g., Diemand et al. 2008). Most of the extant attempts to determine DM radial profiles rely on gas as the dynamical tracer. A number of works have studied nearby disk galaxy kinematics with longslit stellar kinematics to infer DM halo profiles (Corsini et al. 1999; Corbelli & Walterbos 2007) or stellar mass-to-light ratios for isothermal sheet models (van der Kruit & Freeman 1984, 1986; Bahcall & Casertano 1984; Bottema et al. 1987, 1991; Bottema 1989b, 1989a, 1990, 1992; Swaters 1999), but better structure constraints come from two-dimensional spectroscopy (e.g., Copin et al. 2004; Krajnović et al. 2005; Cappellari et al. 2006; van den Bosch et al. 2008; Weijmans et al. 2009; Murphy et al. 2011).

NGC 2976 has made one of the cleanest cases for a cored DM halo via its gaseous kinematics (Simon et al. 2003, hereafter SBLB03). In our first attempt to derive DM mass profiles from stellar kinematics we chose NGC 2976 due to several of its properties. (1) NGC 2976 is an SAc dwarf galaxy in the M81 group. There are some dynamical indications (Spekkens & Sellwood 2007) and photometric indications (Menéndez-Delmestre et al. 2007) that a weak bar may be present, but NGC 2976 is usually given an unbarred designation (de Vaucouleurs et al. 1991). (2) NGC 2976 has some dark patches that are likely due to dust, but its dust content is modest for its Hubble class and distributed rather regularly. A full treatment regarding the potential impact of dust on the measured kinematics is beyond the scope of this work, but several literature

* This paper includes data taken at The McDonald Observatory of The University of Texas at Austin.

estimates of the dust content exist. Williams et al. (2010) fit star formation history models from the broadband colors of resolved stars in the Advanced Camera for Surveys Nearby Galaxy Survey Treasury (ANGST; Dalcanton et al. 2009) by modeling 0.8 mag of differential extinction in the *V*-band for ages above 100 Myr, 0.5 mag for younger ages, and a foreground screen of 0.46 mag. Our data lie within the "INNER-1" region of that work. Prescott et al. (2007) use *Spitzer* 24 μm data to estimate $A_B \sim 1.5$. The lowest estimates come from SBLB03 with $A_B \sim 0.23$ based on an inclination proscription (Sakai et al. 2000). Although there is a large range in the estimated extinctions, the values from each method are on the low end for the late-type dwarf population. (3) NGC 2976 appears to be DM dominated at $r > 500$ pc according to SBLB03 (although de Blok et al. 2008 disagree), so the impact of stellar population synthesis (SPS) mass-to-light (Υ_*) uncertainties is minimized in this target. (4) The stellar surface brightness profiles in many bands are very smooth and indicate a bulgeless disk with a small nuclear star cluster and a break to an outer disk at ∼1.2 kpc (SBLB03).

The distance to NGC 2976 from the tip of the red giant branch method is 3.56 ± 0.38 Mpc (Karachentsev et al. 2002); we adopt a distance of 3.45 Mpc and a scale conversion of 16.7 pc arcsec^{-1} in this work for consistency with SBLB03. The total mass of NGC 2976 is estimated to be $3.5\times10^9\ M_\odot$ based on the inclination-corrected line width of 165 km s^{-1} (SBLB03). The inclination is variously estimated as 61°.5 (de Vaucouleurs et al. 1991), 61°.4 (SBLB03), and 64°.5 (de Blok et al. 2008). The H I heliocentric velocity is 4.0 ± 2.0 km s^{-1} (Stil & Israel 2002b). The stellar velocity dispersion in NGC 2976 has not previously been reported. Measurement attempts were made in Ho et al. (2009), but the results were unresolved in the presence of the best $\sigma_{\rm inst} = 42$ km s^{-1} instrumental resolution and unreported. They estimate $\sigma = 36.0 \pm 16.8$ km s^{-1} from a correlation for their sample with the measured [N II]6583 Å line width.

We present observations of NGC 2976 with the large field-of-view fiber fed Visible Integral field Replicable Unit Spectrograph Prototype (VIRUS-P; Hill et al. 2008) to concurrently measure the gaseous and stellar kinematics, fit mass models, and study the DM halo profile shape in the context of the "core-cusp" controversy with a collisionless tracer. Our data reduction and kinematic measurements are described in Section 2. In Section 3, we investigate the constraints on Υ_* through matching SPS models to our spectral data and its effect on the mass models. We fit the stellar kinematic data with anisotropic Jeans models in Section 4. We perform fits to our [O II] rotation curve and the SBLB03 Hα rotation curve in Section 5. Finally, we review our conclusions in Section 6. As is customary, all values of Υ_* are given in solar units for the indicated band with the "*" indicating a mass exclusively for the stellar component. We adopt an absolute solar magnitude in the *R*-band of $M_{\odot,R} = 4.42$ throughout this work (Binney & Merrifield 1998).

2. OBSERVATIONS AND DATA REDUCTION

Over 2009 April 27 through May 1, we took 18 hr of science pointings on NGC 2976 with the VIRUS-P instrument and the 2400 lines mm^{-1} VP2 grating on the McDonald Observatory's 2.7 m Harlan J. Smith telescope under non-photometric conditions. Transparency was continuously monitored by stars in the guider camera's data, which was read out and saved every 5 s and used to make relative flux calibrations. The seeing ranged from 1″.4–3″.0 full width at half-maximum (FWHM). The VIRUS-P field of view covers 1′.61 × 1′.65 with fibers projected to on-sky diameters of 4″.235. VIRUS-P has a one-third filling factor, so we spread three dithers across the galaxy to maintain continuous spatial coverage in the middle and to maximize the spatial extent. We set the instrument to measure 3680–4400 Å with $R = 2400$, nominally. The spectral data were taken under 1×1 binning, yielding 4 pixels sampling the instrumental FWHM. Individual exposures were of 30 minute duration. We took 20 minute sky nods offset from the galaxy by 10′ between the science data frames. Our best stellar kinematics come from around the *G*-band at 4300 Å and its many surrounding, mostly Fe, features. We also measured the [O II]λλ3726, 3729 lines and all Balmer lines higher than and including Hγ. The data were reduced with the `vaccine` pipeline described in Adams et al. (2011). We have corrected all observations to the heliocentric frame. The instrumental wavelength zero point is observed to drift by ∼10 km s^{-1} over normal swings in nightly operating conditions. We track this and correct the zero point by fitting the 4358.3 Å Hg I skyline in every nodded sky exposure. Quoted wavelengths are not corrected to vacuum conditions.

2.1. Binning

We have, in total, 738 spectra with signal-to-noise (S/N) ranging up to 60 pixel^{-1}. In order to extract reliable stellar velocity dispersions under high S/N conditions, we bin our data as shown in Figure 1. Constant sized bins were chosen for simplicity. The stacks are made with one interpolation to a common, linear wavelength scale considering the different wavelength solutions in each fiber and the individual heliocentric corrections. Membership in a bin was determined solely from each fibers' central position; fibers extended over multiple bins were not given partial weights. We tested extractions using partial weights, and the results agreed to those presented to within the estimated errors. This is expected since the square bins are considerably larger than the fibers, and the usual fractional area that seeps in and out of the square bin for a collection of fibers is only 10%. The spectra were not degraded to have a common instrumental resolution prior to binning. We made this choice to minimize the covariance between spectral channels. Instead, the average instrumental resolution was associated with each bin. We compared the kinematics derived from making resolution-matched stacks and from simply degrading the kinematic template spectra to the average instrumental resolution in each bin. The two methods agreed, on average, and only displayed differences within the estimated errors. Adaptive binning strategies were not adopted, so there is a significant range of S/N in the binned spectra. The mean S/N pixel^{-1} is 29 with a dispersion of 23. We test whether this range in S/N influences our extracted velocities in Section 2.4 and find no impact. In the case of NGC 2976, adaptive spatial binning is not ideal and would lead to the loss of spatial resolution in the outer parts where the contribution of $V_{\rm los}$ to $V_{\rm rms}$ is significant. The analysis of the stellar kinematics is made with these 16″ × 16″ bins, while the analysis of the gas kinematics is made under the native fiber diameters of 4″.235.

2.2. Spectral Resolution

Our observations were taken with an instrumental dispersion of between 40 and 60 km s^{-1} across different fibers and wavelengths. We measure this resolution to 0.5 km s^{-1} uncertainty in every fiber and wavelength with our twilight flats and high-resolution solar spectrum data (Kurucz et al. 1984). Finally, the

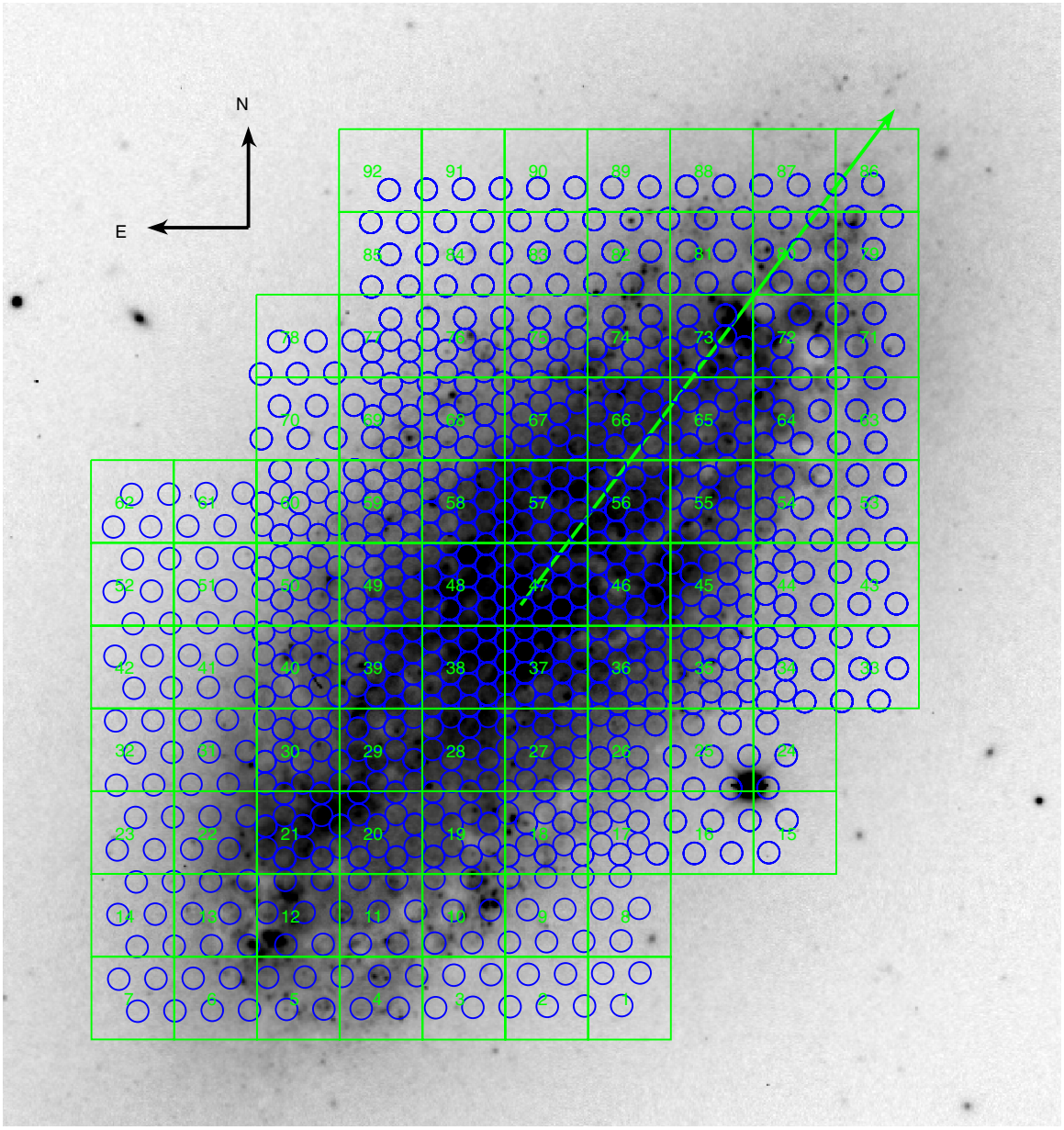

Figure 1. SINGS *R*-band image of NGC 2976 overlaid with the VIRUS-P fiber positions. The numbered squares show the spatial bins used in the extraction of the stellar kinematics. The arrow indicates the major axis with a scale of 120″ (2 kpc at our assumed distance).

(A color version of this figure is available in the online journal.)

binning process combines fibers with different instrumental resolutions, per our dithering scheme. We average the instrumental resolution for each bin. A fit to one fiber is shown in Figure 2. The fit to all bins is summarized in Figure 3. The solutions agree with arc lamp data, although the sparse number of available arc lamp lines leads to a less constrained solution. We also took spectra of a number of template stars (Prugniel & Soubiran 2001) to test our instrumental resolution and find agreement. We experiment with degrading all the data in a bin to the maximum instrumental resolution prior to stacking, but we find differences only at levels far smaller than the formal errors.

2.3. Gaseous Kinematics

We measure the gaseous kinematics through the [O II]λλ3726.032, 3728.815 doublet. Without binning and in each fiber, we simultaneously fit two Gaussian functions over an 18 Å window. Five parameters are fit through a least-squares minimization: the intensities of each emission line, a constant continuum, the radial velocity, and the line width. The best-fit models are perturbed with the estimated flux uncertainties in Monte Carlo realizations to generate velocity uncertainties. The median measured intrinsic line width is $\sigma = 20.4$ km s^{-1} with no strong spatial gradients. We make models of the circular velocity profile from the line-of-sight velocity measurements in Section 5.

2.4. Stellar Kinematics Extraction

We fit the stellar kinematics in each bin with a maximum penalized likelihood estimate of the Gaussian line-of-sight velocity distribution (LOSVD) in pixel space via code described in Gebhardt et al. (2000). We use the empirical, $R = 10k$ stellar templates of Prugniel & Soubiran (2001; ELODIEv3.1)

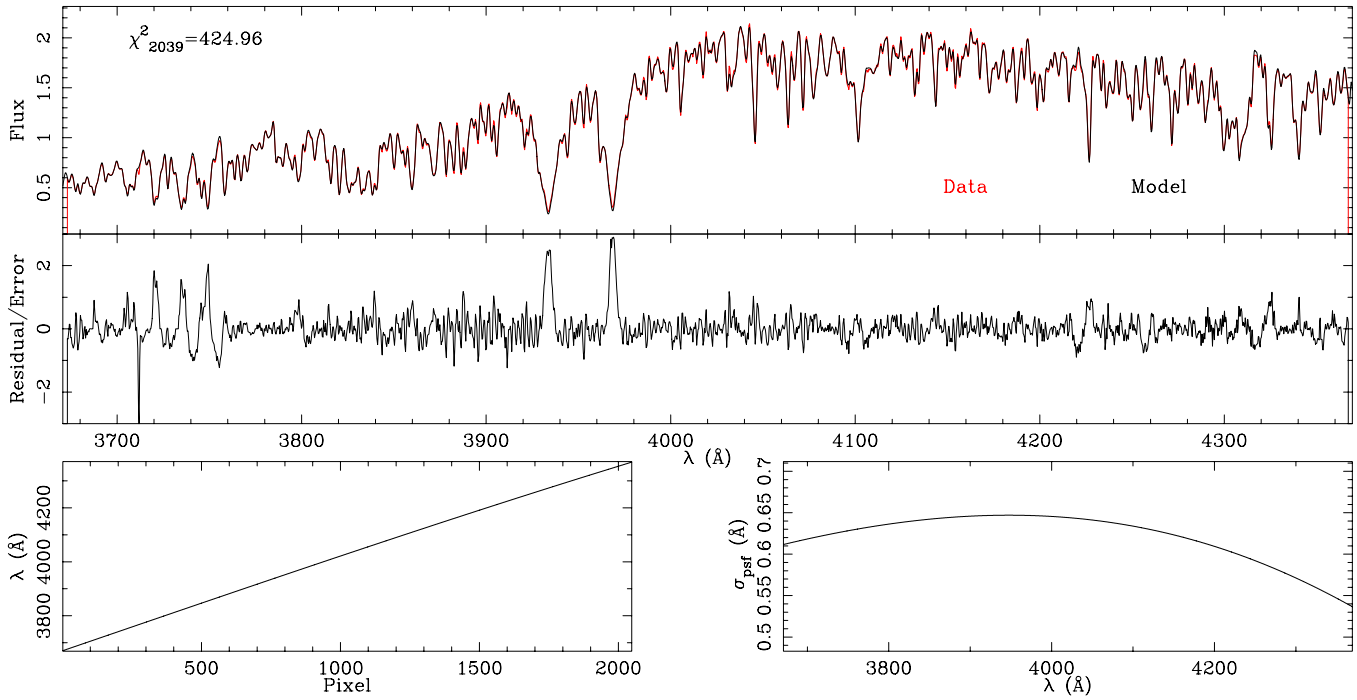

Figure 2. Simultaneous wavelength and instrumental resolution fit for a particular VIRUS-P fiber. The solutions are parameterized by a fourth-order polynomial in wavelength and a third-order polynomial in spectral resolution. The fits are made by matching a higher resolution solar spectrum to twilight flat frames.
(A color version of this figure is available in the online journal.)

Table 1
Kinematic Template Stars

HYPERLEDA	HD	Type	[Fe/H]	Average Weight	Intrinsic σ (km s^{-1})
00672	HD181214	F8III	−0.01	0.086	30.8
01269	HD058923	F0III	0.21	0.185	0
01286	HD062509	K0IIIb	0.02	0.006	11.1
01298	HD068017	G4V	−0.41	0.067	10.6
01322	HD073667	K1V	−0.55	0.032	10.9
01359	HD088609	G5IIIwe	−2.67	0.197	12.3
01366	HD089744	F7V	0.11	0.008	15.3
01733	HD169985	G0III+	0.34	0.138	12.3
01828	HD193793	WC+	0.77	0.280	0

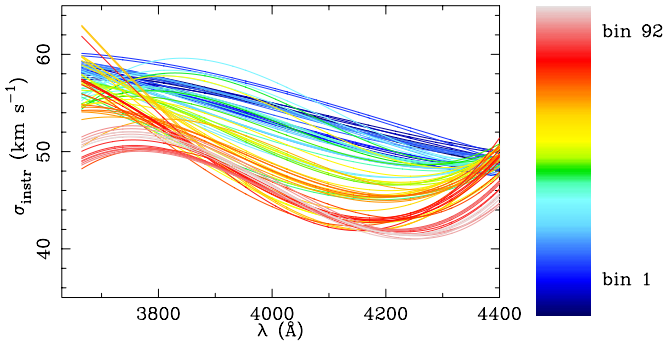

Figure 3. Instrumental resolution in each kinematic extraction bin.
(A color version of this figure is available in the online journal.)

convolved to the instrumental resolution of each bin. All data and templates are normalized prior to convolution by running two boxcars over each spectra. The first boxcar has a 40 Å width. All pixels deviating from the smoothed continuum estimate by $>1.5\sigma$ are masked in the second boxcar, which has a 14 Å width. The specifics of this normalization have little impact, as judged by varying the normalization parameters, on the convolution since both the flux-calibrated VIRUS-P and ELODIE spectra have very shallow slopes over the extracted wavelengths.

The choice of templates is made from amongst the 1959 available, although only a small number are required to describe the data. The membership is determined by manually iterating the list to find a local minimum in root mean square (rms). Several such minima can be found, but the exact choice is unimportant so long as similar stellar types are included. We list our chosen, final set in Table 1. A Wolf-Rayet star takes on a significant weight. However, its only function over this wavelength range is to lower the combined equivalent width of absorption features and is degenerate with, say, the A7m star HD003883. The metallicity has been modeled by ANGST at [M/H] = −0.12 for this region and by imposing a constraint that metallicity grows with time. Most of the F and G giants in our template list have higher metallicity. However, experiments including the template HD148856, a G8III at [Fe/H] = −0.26, do not improve the fit.

Although we track formal uncertainties, we also tally an empirically determined, systematic uncertainty as the rms from

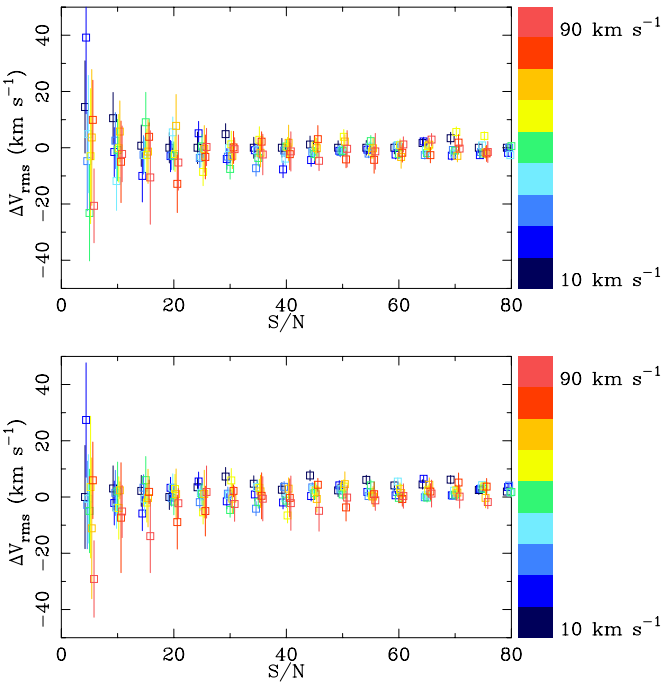

Figure 4. Extracted velocity dispersions in simulated data. The instrumental resolution was set to 50 km s^{-1}, and the color is coded by stellar velocity dispersion. Top: the simulated data came from a subset of the LOSVD template set. No systematics are seen down to very low S/N and dispersions. Bottom: the extracted velocity dispersions in simulated data. The simulated data come from stars in the ELODIE data set which are not contained in our LOSVD template set. This tests for template mismatch. No systematics are seen down to very low S/N and dispersions.

(A color version of this figure is available in the online journal.)

the best-fit model. The two generally agree, expect at high S/N, where template mismatch becomes evident. All further uncertainties are based on the empirical uncertainty, although these may overestimate the actual uncertainty. Uncertainties in velocity are determined by making Monte Carlo realizations of the best-fitting model with simulated noise determined from the residuals.

Tests are run to determine the limits of reliable kinematic extraction under a range of S/N and intrinsic velocity dispersions. First, a subset of the template spectra are combined, then convolved by a simulation dispersion and the instrumental resolution, and noise is added. The extraction of the velocity dispersion is shown in Figure 4. The errors are accurately estimated, and no systematic effects are seen down to S/N > 5 and $\sigma > 10$ km s^{-1}. Next, a similar test is made to capture the possibility of template mismatch. We combine the ELODIE templates for HD000432, HD068380, and HD081809 in a 21:53:27% ratio. The stars are not part of our fitting template, but they have similar spectral types. The extractions of velocity dispersion are shown again in Figure 4. The errors are marginally larger, but again they are accurately estimated and without systematic trends.

Representative spectra and their best-fit models are given in Figure 5. Several additional corrections are made. The instrumental resolution uncertainty, estimated as 0.5 km s^{-1}, is propagated as a random error to V_{rms} along with the statistical errors. The ELODIE headers quote broadening of the stellar features for some stars beyond their $R = 10k$ resolution; we are not certain whether this broadening is physical, such as by binaries, or a spurious artifact. The average value for our templates is $\sigma = 5.2$ km s^{-1}. We treat the broadening as physical and subtract off the ELODIE instrumental resolution and the average broadening in quadrature from our VIRUS-P instrumental resolution prior to template convolution. However, the effect is small compared to the final uncertainties. Additionally, the systemic velocity is estimated directly from our data. The inverse-variance-weighted average of our stellar bins is 4.60 km s^{-1}, consistent with an earlier optical determination of 3 ± 5 km s^{-1} (de Vaucouleurs et al. 1991) and the H I measurement of 4 ± 2 km s^{-1} (Stil & Israel 2002b). This is subtracted from the

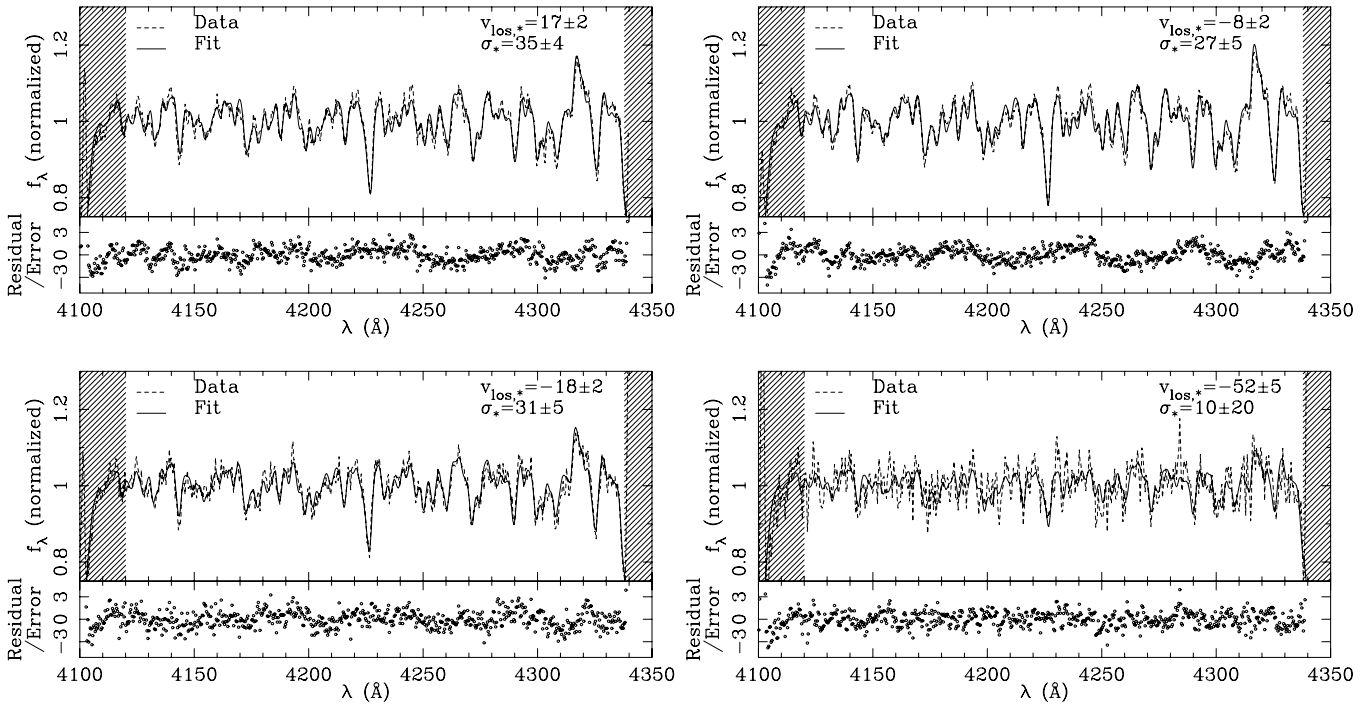

Figure 5. Spectra and fits in several bins. The chosen bins (56, 38, 19, and 5) represent a range of S/N (57, 57, 53, and 26) starting from the top left going clockwise. The error normalized residuals are shown in the bottom panel.

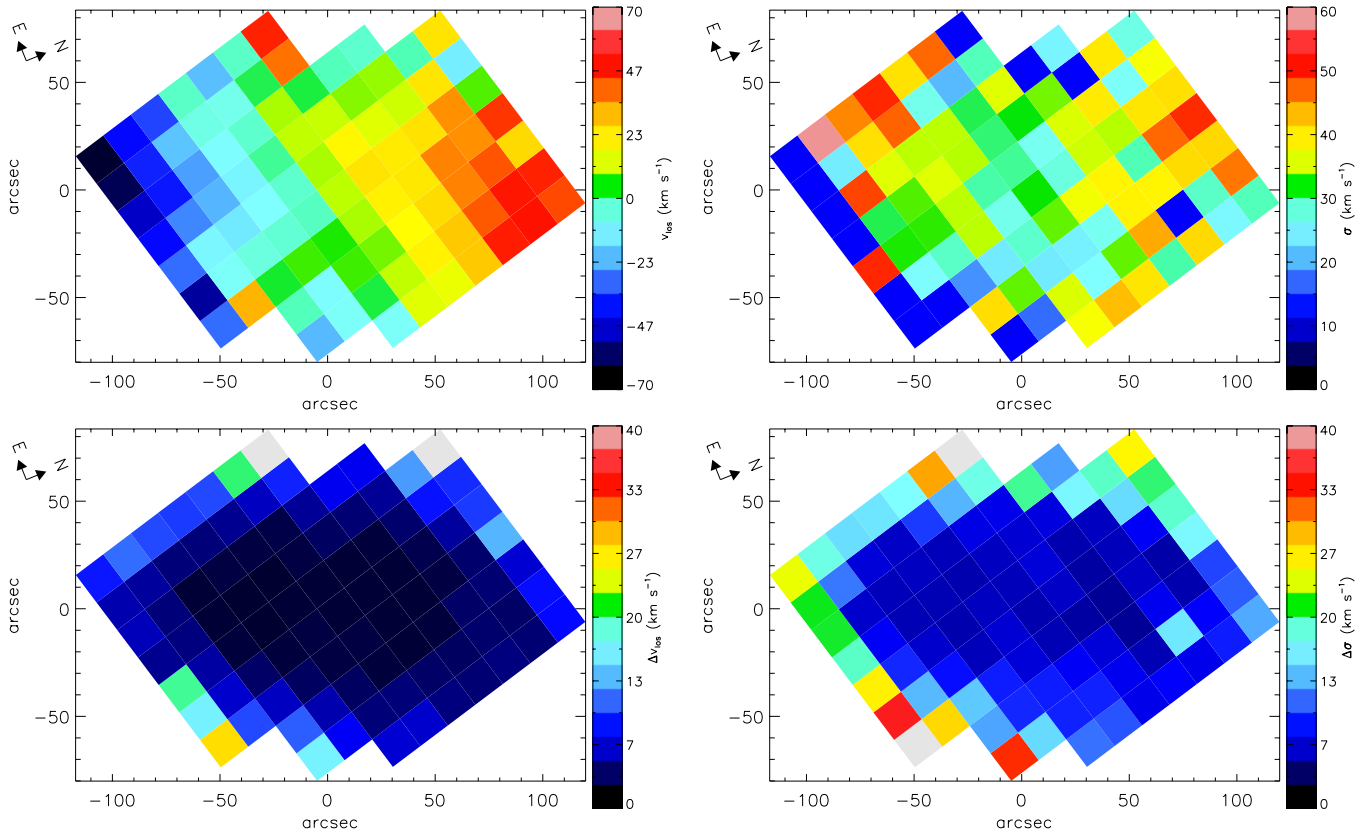

Figure 6. Velocity maps for NGC 2976. Top left: the stellar line-of-sight velocity map. Bottom left: the line-of-sight velocity error map. Top right: the stellar velocity dispersion map. The data are consistent with a flat or only modestly sloped velocity dispersion profile. Bottom right: the stellar velocity dispersion error map.
(A color version of this figure is available in the online journal.)

line-of-sight velocities before forming $V_{\rm rms}$. The line-of-sight velocity and velocity dispersion for each bin, with uncertainties, are given in Table 2. Figure 6 shows the maps of line-of-sight velocity, velocity dispersion, and uncertainties that we measure from the data. The final velocity dispersions are not allowed to fall below 10 km s^{-1} in order for their error estimates to impact the error on $V_{\rm rms}$. This is consistent with the lowest velocity dispersions that we can reliably extract in simulated data.

Jeans models make predictions for the projected, second velocity moment. For a Gaussian kernel, the second moment is simply $V_{\rm rms} = \sqrt{V_{\rm los}^2 + \sigma^2}$. The chosen spectral window fit is 4110 Å $< \lambda <$ 4340 Å, which includes the G-band, a strong Ca absorption line at 4227 Å (Worthey et al. 1994), and a large number of weak Fe features. Fits to the spectral window 3980 Å $< \lambda <$ 4100 Å give similar measurements, but they are noisier due to the smaller bandpass and less prominent features. We show the consistency between spectral regions in Figure 7.

A careful viewing of the velocity dispersion map in Figure 6 shows a profile that is nearly flat, but perhaps contains higher velocity dispersions in the northerly direction. This pattern remains whether we remeasure the instrumental resolution within each night's data or adopt a resolution fixed with time. However, the evidence for a velocity dispersion gradient is within the noise.

3. STELLAR POPULATION SYNTHESIS CONSTRAINTS

A loose but independent estimate on Υ_* can be made by comparing stellar population models to spectral energy distribution (SED) data, either photometrically (e.g., Bell & de Jong 2001) or spectrophotometrically. Substantial systematic uncertainties in, for instance, the initial mass function (IMF) and the properties of thermally pulsing asymptotic giant branch (TP-AGB) stars (e.g., Maraston 2005) at NIR wavelengths limit the precision of Υ_* constraints from SED fits. Experiments designed to provide optimal observational constraints on stellar Υ_*'s by applying isothermal sheet relations are underway (Herrmann & Ciardullo 2009; Bershady et al. 2010a, 2010b), but the goal of this work is instead to model and fit all mass components simultaneously. Specific to NGC 2967, SBLB03 found tension in the maximal disk value of $\Upsilon_{*,K} < 0.09^{+0.15}_{-0.08}$ compared with the higher values implied by some SED fits (one of their models has $\Upsilon_{*,K} = 2$).

We analyze the stellar population by fitting spectra with SPS models from Bruzual & Charlot (2003) and the preliminary release of their 2007 version that incorporates new TP-AGB values (Bruzual 2007). We use the Padova 1994 (Alongi et al. 1993; Bressan et al. 1993; Fagotto et al. 1994a, 1994b; Girardi et al. 1996) and Marigo 2007 (Marigo & Girardi 2007) evolutionary tracks, respectively. Both Chabrier and Salpeter IMFs are tried, which represent reasonable lower and upper bounds on Υ_*. To achieve robust star formation histories, we use the same 39 templates as Tremonti et al. (2004), which entail combinations of three metallicities ($Z = 0.2, 1, 2.5\, Z_\odot$) and a variety of star formation histories (instantaneous bursts of age 0.005, 0.025, 0.10, 0.29, 0.64, 0.90, 1.4, 2.5, 5, and 11 Gyr; a 6 Gyr old population under a constant star formation rate, and two tau models sampled at a 12 Gyr age with $\tau_{\rm SFR} = 5, 9$ Gyr). We further add a grid of dust extinction with the form of Calzetti et al. (2000) over 21 values of $E_s(B-V)$ uniformly spaced from 0 to 1. We resample our spectra to the rest frame, convolve the templates to match the 8 Å FWHM Spitzer Infrared Nearby

Table 2
Stellar Kinematic Measurements in NGC 2976[a]

Bin [b]	Major Axis Distance (″)	Minor Axis Distance (″)	$v_{los,*}$ (km s^{-1})	$v_{los,*}$, 1σ Uncertainty (km s^{-1})	σ_* (km s^{-1})	σ_*, 1σ Uncertainty (km s^{-1})
1	−48.1	−62.5	−34.53	26.29	10.00	49.63
2	−57.7	−49.7	−55.44	15.52	10.00	34.29
3	−67.3	−37.0	−34.53	18.81	48.27	24.73
4	−76.9	−24.2	−45.49	3.90	10.00	18.03
5	−86.5	−11.4	−51.80	5.01	10.00	19.68
6	−96.2	1.3	−62.00	4.67	10.00	19.78
7	−105.8	14.1	−65.17	7.47	10.00	23.18
8	−35.3	−52.9	27.51	9.08	10.00	26.72
9	−44.9	−40.1	−11.36	5.43	24.54	12.43
10	−54.5	−27.3	−14.32	4.37	30.58	7.89
11	−64.2	−14.6	−32.05	3.31	29.10	6.55
12	−73.8	−1.8	−43.70	3.18	46.88	5.49
13	−83.4	11.0	−42.71	4.22	22.76	10.50
14	−93.0	23.8	−45.30	10.15	56.69	17.22
15	−3.3	−68.8	−26.18	15.56	10.00	32.14
16	−12.9	−56.0	−6.00	9.61	39.36	11.88
17	−22.5	−43.2	−1.24	5.14	16.88	12.89
18	−32.1	−30.5	−9.45	2.73	26.91	7.21
19	−41.8	−17.7	−18.39	1.71	30.71	5.34
20	−51.4	−4.9	−26.85	1.43	31.07	4.85
21	−61.0	7.9	−29.12	1.50	34.13	4.89
22	−70.6	20.6	−25.46	3.28	39.24	5.65
23	−80.3	33.4	−39.14	9.02	43.85	13.96
24	9.5	−59.1	−11.57	6.45	15.23	13.59
25	−0.1	−46.4	−12.83	4.69	31.38	7.91
26	−9.7	−33.6	1.99	2.61	22.52	7.57
27	−19.4	−20.8	−8.08	1.64	32.75	4.94
28	−29.0	−8.0	−12.27	1.40	32.78	4.62
29	−38.6	4.7	−14.64	1.35	34.33	4.71
30	−48.3	17.5	−12.42	1.73	32.77	5.03
31	−57.9	30.3	−9.70	3.21	45.44	5.29
32	−67.5	43.1	−7.36	8.60	48.44	14.59
33	31.9	−62.3	−11.61	5.59	35.13	10.25
34	22.3	−49.5	−1.60	3.29	33.96	7.72
35	12.7	−36.7	1.96	2.54	22.54	7.65
36	3.0	−24.0	1.11	1.85	26.62	5.67
37	−6.6	−11.2	−6.59	1.73	25.43	5.62
38	−16.2	1.6	−7.58	1.54	27.82	5.04
39	−25.9	14.4	−4.36	1.32	32.51	4.59
40	−35.5	27.2	−7.92	1.84	32.87	4.89
41	−45.1	39.9	−10.69	3.90	25.57	8.49
42	−54.7	52.7	−26.01	8.98	38.92	16.60
43	44.7	−52.7	9.80	5.35	41.22	9.30
44	35.1	−39.9	7.40	3.25	24.71	7.73
45	25.4	−27.1	3.85	1.69	23.17	6.58
46	15.8	−14.3	5.60	1.86	31.52	4.77
47	6.2	−1.5	6.45	1.43	30.24	4.65
48	−3.5	11.2	5.29	1.50	28.17	4.99
49	−13.1	24.0	7.00	1.74	28.55	5.06
50	−22.7	36.8	5.31	1.93	29.17	6.11
51	−32.4	49.6	−2.15	5.02	18.75	12.36
52	−42.0	62.4	−7.00	19.10	45.28	28.29
53	57.5	−43.0	11.07	3.43	38.57	6.14
54	47.8	−30.2	15.94	2.74	31.43	6.30
55	38.2	−17.5	13.44	1.52	25.29	5.70
56	28.6	−4.7	16.54	1.54	34.99	4.28
57	18.9	8.1	20.57	1.43	26.04	5.32
58	9.3	20.9	14.82	1.53	25.41	5.78
59	−0.3	33.7	7.83	2.53	29.96	5.51
60	−10.0	46.4	−1.65	4.03	34.12	6.17
61	−19.6	59.2	34.47	7.82	27.31	17.13
62	−29.2	72.0	43.28	66.67	10.00	44.09
63	70.2	−33.4	25.36	3.12	27.98	6.72
64	60.6	−20.6	25.45	2.55	42.12	4.86

Table 2
(Continued)

Bin [b]	Major Axis Distance (″)	Minor Axis Distance (″)	$v_{los,*}$ (km s^{-1})	$v_{los,*}$, 1σ Uncertainty (km s^{-1})	σ_* (km s^{-1})	σ_*, 1σ Uncertainty (km s^{-1})
65	51.0	−7.8	22.35	1.68	36.79	4.00
66	41.3	5.0	19.14	1.46	36.58	4.02
67	31.7	17.7	18.32	1.47	33.43	4.37
68	22.1	30.5	9.92	1.62	34.08	4.60
69	12.4	43.3	4.18	3.05	31.55	5.96
70	2.8	56.1	−5.93	6.36	10.00	18.74
71	83.0	−23.8	44.14	3.44	39.98	6.14
72	73.4	−11.0	37.15	2.95	10.00	14.62
73	63.7	1.8	32.91	2.67	36.58	6.40
74	54.1	14.6	32.88	1.79	27.56	5.30
75	44.5	27.4	20.85	2.07	32.52	4.91
76	34.8	40.2	7.99	2.92	37.76	5.12
77	25.2	53.0	5.11	4.08	10.00	15.89
78	15.6	65.7	−7.83	6.33	23.54	11.61
79	95.8	−14.1	44.77	3.09	24.18	7.57
80	86.2	−1.3	44.70	2.81	26.93	6.62
81	76.5	11.4	37.63	3.08	39.61	4.68
82	66.9	24.2	31.54	2.88	45.35	4.49
83	57.3	37.0	31.35	4.23	38.50	6.47
84	47.6	49.8	19.65	7.23	25.00	13.79
85	38.0	62.6	−5.33	11.58	37.91	17.95
86	108.6	−4.5	38.98	7.02	27.43	11.96
87	98.9	8.3	43.17	7.08	44.62	9.69
88	89.3	21.1	22.96	5.53	40.10	8.91
89	79.7	33.9	40.93	12.32	48.21	16.14
90	70.0	46.7	2.96	8.51	39.16	17.83
91	60.4	59.4	−16.52	8.01	35.10	19.13
92	50.7	72.2	20.40	40.00	25.82	24.16

Notes.
[a] Column 4 contains the systemic velocity which we measure as a weighted average to be 4.60 km s^{-1}. The quantity fit in the Jeans models is the velocity second moment (V_{rms}), or the sum in quadrature of Columns 4 and 6 with the systematic velocity removed. The V_{rms} error is formed by the propagation of the listed terms as well as an estimated 0.5 km s^{-1} uncertainty on the average 50 km s^{-1} instrumental resolution.
[b] The central position of each bin is given. The bins are 16″ × 16″ in size and rotated by −53° east of north.

Galaxies Survey (SINGS) instrumental resolution, and mask out windows 4 Å wide around each of the Balmer lines, [O II] and [Ne III]3869. Repeated observations of spectrophotometric standards stars with VIRUS-P have shown the relative flux calibration to be accurate to better than 10% (Adams et al. 2011). The match to the SINGS 20″ × 20″ drift-scan spectrum is excellent, as shown in Figure 8. Due to the larger bandpass, we quote values by fitting to the SINGS spectrum. Similar, but less constrained, values are obtained from the VIRUS-P data. The templates' normalizations are fit through least-squares minimization, first individually and then in all 334,971 two-component combinations from the metallicity, star formation history, and dust grids. The relative probability of each model is calculated as $\exp(-\chi^2/2)$ (e.g., Kauffmann et al. 2003). All quoted Υ_* values include the effects of dust. The 1σ confidence intervals centered on the highest probability $\Upsilon_{*,R}$ are 0.63 ± 0.39, 1.23 ± 0.52, 1.04 ± 0.23, and 1.42 ± 0.42 for the BC03/Chabrier, BC03/Salpeter, CB07/Chabrier, and CB07/Salpeter models, respectively. Given the tight ranges from the statistical errors alone, the Υ_* uncertainty is dominated by systematic uncertainties. We consider $\Upsilon_{*,R} = 1.1 \pm 0.8$, the mean and the symmetric uncertainty that encompasses the 1σ confidence intervals for all four estimates, as the best spectrophotometric limit; therefore we present mass models with $\Upsilon_{*,R}$ both freely fit and penalized by this conservative confidence interval in Sections 4.3 and 5.

Finally, we investigate the Υ_* limits enabled by broadband photometry. We use the optical through Two Micron All Sky Survey data points of SBLB03 by assuming 10% errors and two Infrared Array Camera data points of Dale et al. (2007) for NGC 2976 without any aperture corrections as shown in Figure 9. The same stellar population models are fit through the EAZY package (Brammer et al. 2008). The best-fit value of Υ_* is consistent with our spectral fits. However, it is starkly inconsistent with the SPS value used by de Blok et al. (2008) and calibrated in Oh et al. (2008) that renders NGC 2976 to be dominated by the baryonic mass. The relation derived there is based on SPS models that have aged 12 Gyr and does not match the observed colors of NGC 2976. Our fit to the SED suggests $\Upsilon_{*,R} = 0.64$ and $\Upsilon_{*,3.6\,\mu m} = 0.18$, while the de Blok et al. (2008) model gives $\Upsilon_{*,3.6\,\mu m} = 0.66$.

4. JEANS MODELS

The minimally necessary components to the NGC 2976 mass model are a stellar disk with a spatially uniform mass-to-

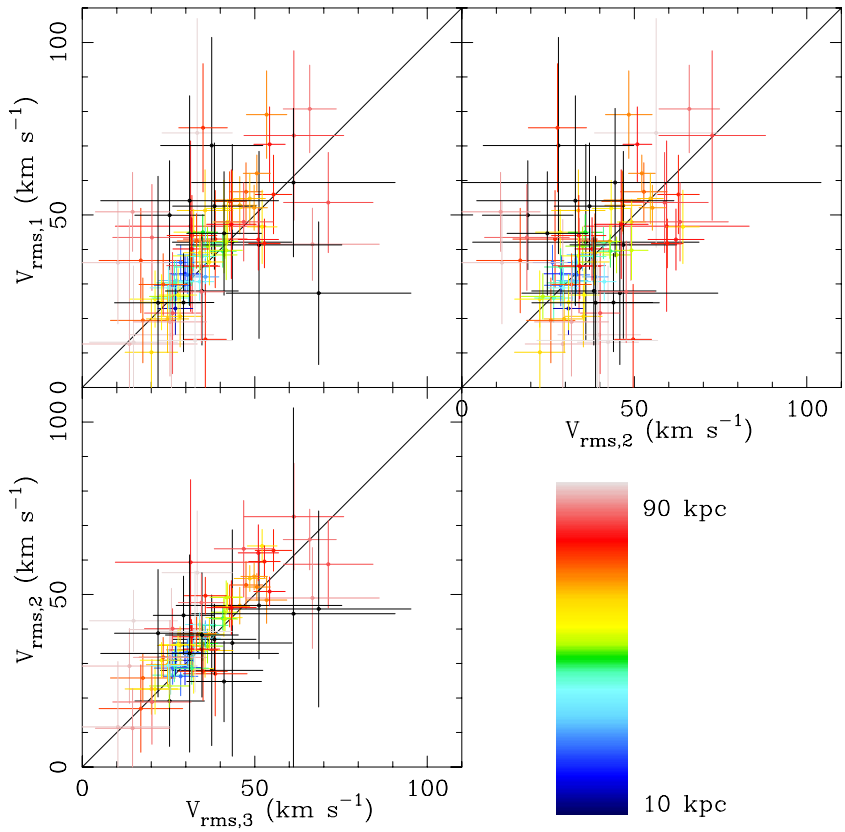

Figure 7. rms velocity as measured in various spectral windows. The values are color coded by their distance along the major axis. The first, second, and third labels refer to the 3900 Å $< \lambda <$ 4100 Å, 4100 Å $< \lambda <$ 4340 Å, and joint windows, respectively. The estimates generally agree, especially for the high S/N data points which drive the modeling. We use the 4100 Å $< \lambda <$ 4340 Å kinematics as the preferred value due to the lower errors and the more homogenous instrumental resolution compared to the joint range.

(A color version of this figure is available in the online journal.)

light ratio, atomic hydrogen, and a DM halo under a power-law parameterization. We use extant photometry to infer the distribution of the first two, and we use kinematic measurements and Jeans model solutions to infer the latter.

4.1. H I Deprojection

We use the robust weighting ($\mathcal{R} = +0.5$), zeroth moment map of 21 cm atomic hydrogen in NGC 2976 from The H I Nearby Galaxy Survey (THINGS; Walter et al. 2008) to characterize the H I mass model. The H I distribution is highly clumped around the two off-center star-forming complexes and unlikely to be axisymmetric. Nevertheless, we perform Multi-Gaussian Expansion (MGE; Emsellem et al. 1994; Cappellari 2002) fits to the data, subject to the axisymmetric limitations of this work's modeling, and calculate a resultant circular velocity profile (Appendix A, Cappellari 2002). SBLB03 have shown that H I is a dynamically somewhat important component at $r > 80''$, but that H_2 (from CO measurements) is a minor contributor to the gravitational potential at all radii. Therefore, we neglect the molecular component. SBLB03 fit the H I from an older data set (Stil & Israel 2002a) and by assuming an infinitely thin disk; they present a circular velocity profile that is in general a factor of two times larger than our derived values. We apply the MGE mass model to the fits of Sections 4.3 and 5, although the presence of the H I component does not strongly influence our final results. The contribution from H I to the circular velocity is given in Table 3.

Table 3
Rotation Curve Data

Radius (arcsec)	$v_{c,\mathrm{TR,[O\,II]}}$[a] (km s^{-1})	$v_{c,\mathrm{HD,[O\,II]}}$[a] (km s^{-1})	$v_{\mathrm{rad,[O\,II]}}$ (km s^{-1})	$v_{c,*}$[b] (km s^{-1})	$v_{c,\mathrm{H\,I}}$ (km s^{-1})
14.1	15.6 ± 0.8	10.6 ± 0.8	5.2 ± 0.4	9.5	1.5
19.1	32.4 ± 0.5	24.6 ± 1.0	9.0 ± 0.6	11.2	2.0
24.1	39.4 ± 0.9	31.4 ± 2.5	11.0 ± 0.7	13.0	2.5
29.1	45.7 ± 0.8	32.1 ± 1.6	6.4 ± 1.5	15.0	3.0
34.1	40.0 ± 0.4	32.4 ± 5.9	6.7 ± 1.6	16.9	3.5
39.1	43.5 ± 1.1	39.7 ± 2.9	7.4 ± 1.8	18.8	3.9
44.1	51.6 ± 0.6	44.7 ± 3.3	2.0 ± 1.8	20.5	4.4
49.1	55.9 ± 0.7	47.7 ± 3.3	3.8 ± 1.3	22.1	4.9
54.1	59.7 ± 1.0	51.7 ± 0.8	3.3 ± 1.0	23.5	5.3
59.1	56.2 ± 0.5	51.0 ± 2.8	2.5 ± 5.5	24.8	5.7
64.1	57.3 ± 0.2	53.7 ± 0.4	-0.3 ± 0.9	25.9	6.1
69.1	63.4 ± 0.3	61.8 ± 0.8	-2.2 ± 2.1	26.8	6.5
74.1	66.7 ± 0.4	64.4 ± 0.8	0.1 ± 1.1	27.6	6.9
79.1	69.9 ± 0.2	72.4 ± 4.8	-4.0 ± 2.3	28.2	7.2
84.1	75.6 ± 0.5	73.8 ± 0.9	-3.5 ± 2.7	28.7	7.6
89.1	73.7 ± 0.5	75.5 ± 3.2	-6.7 ± 5.3	29.0	7.9
94.1	71.3 ± 0.6	68.9 ± 1.6	-4.2 ± 2.1	29.2	8.2
99.1	79.9 ± 0.5	78.1 ± 13.8	-17.2 ± 10.0	29.4	8.5
104.1	80.5 ± 0.9	82.5 ± 8.4	-14.8 ± 7.7	29.4	8.7
109.1	74.5 ± 2.1	69.0 ± 10.9	-10.8 ± 3.8	29.3	9.0

Notes.
[a] The listed errors are statistical. The rms velocities from the best-fit TR and HD models are 4.5 km s^{-1} and 6.1 km s^{-1} for $\Upsilon_{*,R} = 0$, 4.4 km s^{-1} and 6.4 km s^{-1} for $\Upsilon_{*,R} = 1.1$, and 4.5 km s^{-1} and 6.0 km s^{-1} for a freely fit $\Upsilon_{*,R}$, respectively.
[b] Assuming $\Upsilon_{*,R} = 1$. This column scales as $\propto (\Upsilon_{*,R})^{1/2}$.

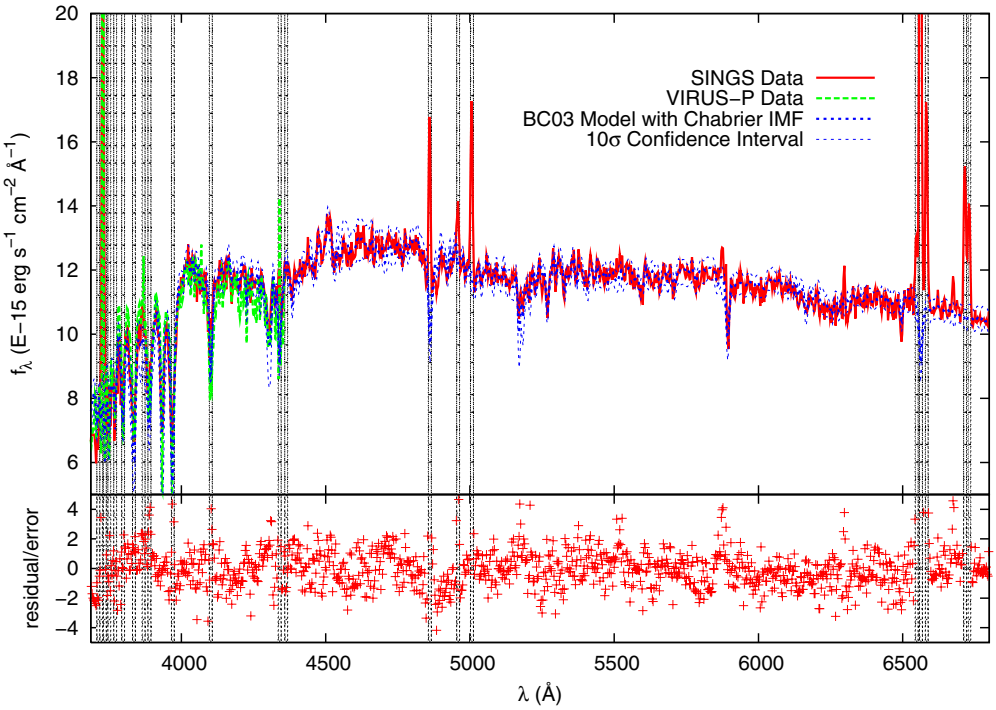

Figure 8. Data and fits to synthetic stellar population models. The spectra have been corrected for their radial velocity, broadened appropriately, and stacked. The SINGS spectrum has poorer resolution than the SPS models, so the SPS models are broadened to match. The average S/N pixel^{-1} over the displayed data is 60. Regions with emission lines have been masked in the fit and shaded in gray hatches. The best two-component model is shown with confidence intervals. Our VIRUS-P data agree well in absolute and relative flux calibration with the SINGS spectrum. The SPS fit is made to the SINGS spectrum, preferred by its wider bandpass and better coverage of the 4000 Å break. The displayed best-fit model proscribes $\Upsilon_{*,R} = 0.90$ with luminosity weighted fractions of 0.91:0.09 for a $Z = 0.2\,Z_\odot$, $E_s(B-V) = 0$, $\tau_{\rm SFR} = 5$ Gyr, 12 Gyr age model and a $Z = 0.2\,Z_\odot$, $E_s(B-V) = 0.60$, instantaneous burst, 25 Myr age model, respectively.

(A color version of this figure is available in the online journal.)

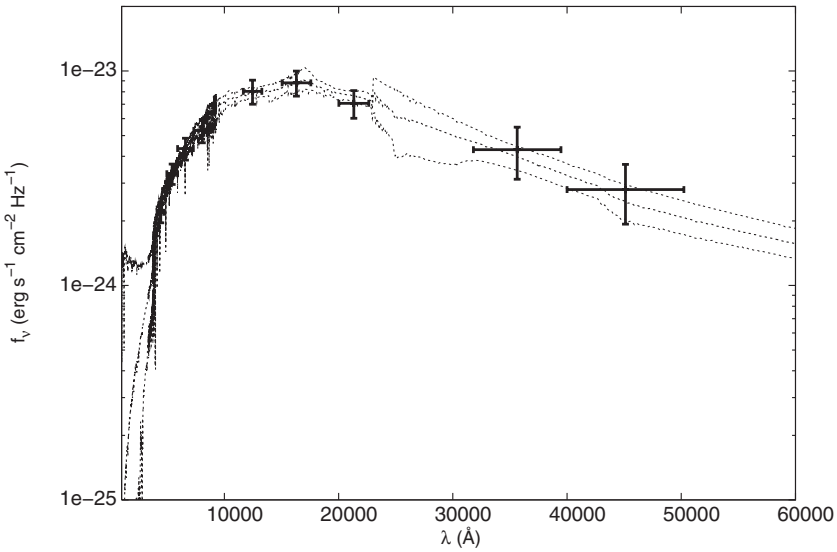

Figure 9. Stellar population fits to the optical and NIR data. The fits predict mass-to-light ratios that are consistent with, but more loosely constrained than, the fit to the SINGS spectrum. The mass modeling of de Blok et al. (2008) uses the 3.6 μm photometry and a color relation derived from Oh et al. (2008) for a value of $\Upsilon_{*,3.6\,\mu{\rm m}} = 0.66$ and claims that NGC 2976 is baryon dominated. Note that this relation was based on stellar populations aged to 12 Gyr and does not match the observed $K-[3.6\,\mu{\rm m}]$ color of NGC 2976. Our models, specifically fit to the spectrophotometry of NGC 2976, disagree. We show the best-fit model and confidence interval with various two-component SPS models. The best-fit model shown proscribes $\Upsilon_{*,R} = 0.64$ and $\Upsilon_{*,3.6\,\mu{\rm m}} = 0.18$ with luminosity weighted fractions of 0.67:0.33 for a $Z = 0.2\,Z_\odot$, $E_s(B-V) = 0.40$, instantaneous burst, 100 Myr age model and a $Z = 0.2\,Z_\odot$, $E_s(B-V) = 0$, instantaneous burst, 2.5 Gyr age model, respectively.

4.2. Stellar Deprojection

We use the *R*-band image taken at the Kitt Peak National Observatory's 2.1 m telescope from the SINGS (Kennicutt et al. 2003) to model the stellar mass distribution. The MGE fit is shown in Figure 10 with the terms listed in Table 4. The MGE model fits both the nuclear star cluster and the inner and outer disks well. The inferred vertical-to-radial scale length is 1:8 at a nominal $i = 63^\circ$ over most of the radial range, although it is near-circular for the nuclear star cluster. Strong color gradients are not seen in NGC 2976 (SBLB03), so we limit our analysis to a single value of $\Upsilon_{*,R}$ for all components. There is some debate

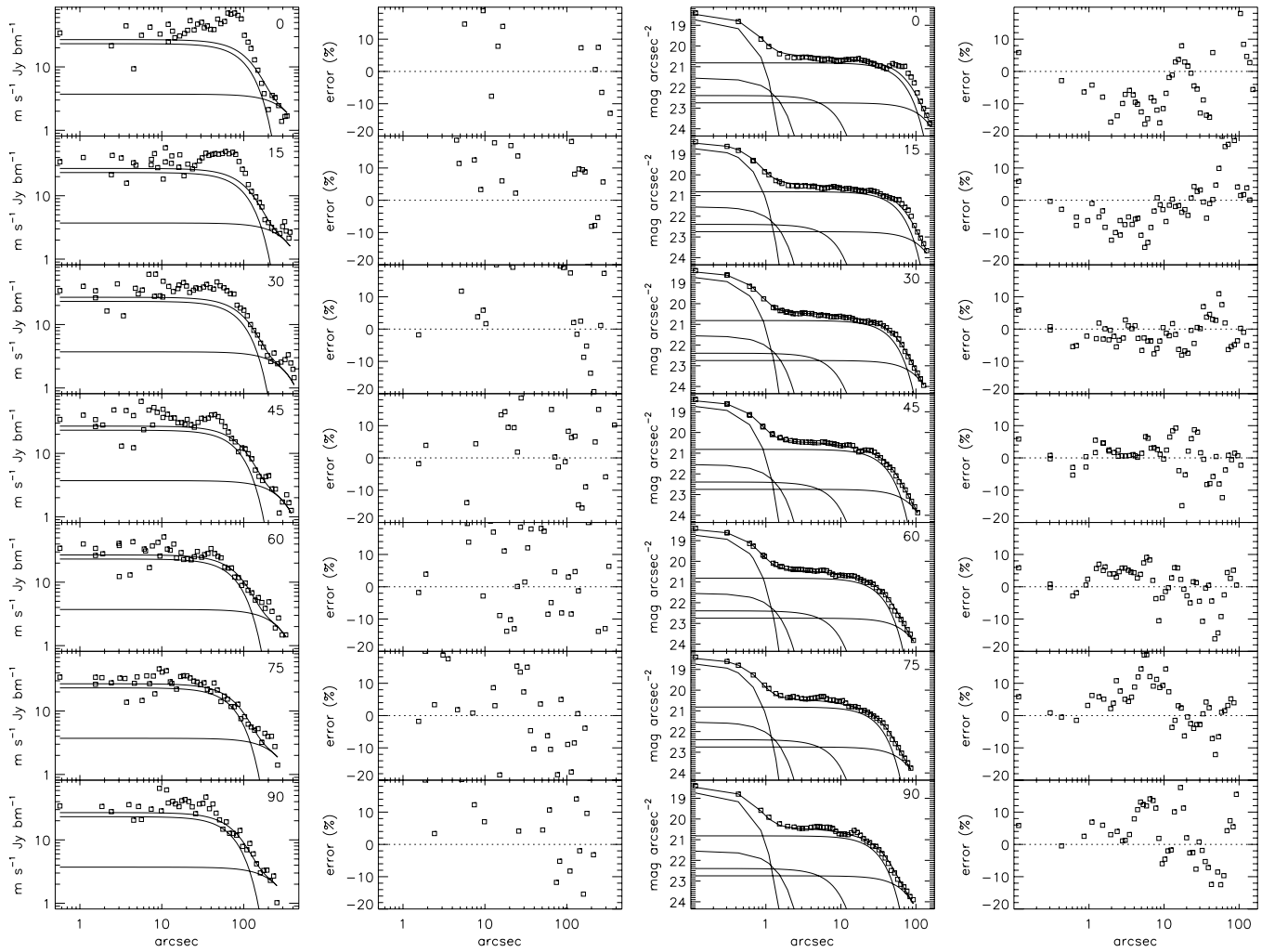

Figure 10. Sector photometry of NGC 2976, folded into one quadrant, with the Multi-Gaussian Expansion (MGE) fit also shown. The values in the upper right of the profile plot indicate the angle from the major axis, in degrees, for each displayed cut. Left: the H I distribution is strongly asymmetric and requires some negative mass components in the model's central regions for a quality fit. To maintain a physical density, we have instead made a poorer fit with only positive components. However, the total H I mass is significantly smaller than the stellar and DM mass, and its inclusion or exclusion does not strongly alter the DM halo fits. Right: the *R*-band data and fit. The nuclear stellar cluster and the break between inner and outer disk near $r \sim 70''$ on the major axis and $r \sim 25''$ on the minor axis are captured in the fit. The two star-forming regions near $r \sim 70''$ on the major axis remain as residuals since they are asymmetric.

Table 4
Multi-Gaussian Expansion Terms for NGC 2976

Component	Index (k)	$\Sigma_{0,k}$ ($M_\odot$ pc^{-2})	σ_k (arcsec)	q'^{a}_k
Stellar[b]	1	2298.3	0.28	1.00
	2	68.9	0.99	1.00
	3	27.8	6.36	1.00
	4	117.8	49.89	0.48
	5	19.6	108.26	0.54
H I	1	8.0	84.80	0.70
	2	1.3	291.13	0.75

Notes.
[a] Observed axial ratio.
[b] *R*-band and assuming $\Upsilon_* = 1$ for this listing.

as to the best filter to use for accurate recovery of stellar mass. TP-AGB stars and polycyclic aromatic hydrocarbons disfavor the NIR. Dust extinction, varieties of star formation history, and nebular emission disfavor the optical. The studies on NGC 2976 of SBLB03 and de Blok et al. (2008) used K_s and *Spitzer* 3.6 μm data, respectively. Portinari et al. (2004) advocate *i*-band photometry and Zibetti et al. (2009) calibrate for combinations of *i*- and *H*-band photometry. We chose to use the available *R*-band image primarily for its depth and resolution in this work. However, that our fits to the SED are consistent across multiple bandpasses (Section 3) means this choice is unimportant for the analysis of NGC 2976.

4.3. Best-fitting Dark Matter Halo

We use the Jeans Anisotropic MGE modeling package (JAM; Cappellari 2008) to fit the binned stellar kinematic field in NGC 2976 in lieu of more computationally intensive Schwarzschild modeling (Schwarzschild 1979). The fits are made to the projected, second-moment velocity ($V_{\rm rms} = \sqrt{V_{\rm los}^2 + \sigma^2}$). We make models assuming a single anisotropy parameter ($\beta_z = 1 - (\sigma_z/\sigma_R)^2$) and a spatially constant Υ_*. The spherical DM halo's radial profile is approximated as a power law

$$\rho(r) = \rho_0 \times (r/1\ {\rm pc})^{-\alpha} \quad (1)$$

while the NFW function has the form of

$$\rho(r) = \frac{\rho_i}{(r/r_s)(1+r/r_s)^2}, \quad (2)$$

with r_s being a scale radius and ρ_i being a density related to the critical density and the halo overdensity.

The power-law approximation is justified since the core radius of NGC 2976 is likely to lie at $r_s \sim 2.5$ kpc (SBLB03, Appendix B), and our stellar data do not extend into the asymptotic region of the rotation curve. This choice also aids comparison to previous work, whereas SBLB03 also used this parameterization and most models for NGC 2976 in de Blok et al. (2008) minimized to solutions with lower limits on radial scale parameters that then reduce to the power-law form. We place the JAM code within a nonlinear least-squares minimization package (`MPFITv.1.64`[7]) to reach our optimal solutions.

The best-fit, five-parameter model has a shallow minimum at $\Upsilon_{*,R} = 3.49$, $i = 63.^\circ3$, $\beta_z = 0.432$, $\rho_0(r = 1\,\mathrm{pc}) = 0.260\,M_\odot\ \mathrm{pc}^{-3}$, and $\alpha = 0.235$ at $\chi^2_{\nu=87} = 77.0$. The second-moment model and residuals are shown in Figure 11. The enclosed mass distribution for this model is shown in Figure 12. The anisotropy we measure is larger than the $\beta_z \sim 0.3$ commonly fit by the same method in E's and SO's (Cappellari et al. 2007; Thomas et al. 2009) and slightly below the $\beta_z \sim 0.5$–0.8 range commonly found in large spirals (van der Kruit & de Grijs 1999; Shapiro et al. 2003; Bershady et al. 2011). We test an isotropic solution as well and find a similar solution in the remaining parameters. The kinematically determined inclination is marginally above the value in de Vaucouleurs et al. (1991) based on photometric ellipticity ($i = 61.^\circ5$). However, we find $i = 64.^\circ6 \pm 1.^\circ5$ from our [O II] tilted ring (TR) [O II] fit Section 5, so the kinematically determined value is reasonable. Inclinations are often poorly constrained by kinematic fits (Krajnović et al. 2005) and can have a strong degeneracy with β_z. There is tension in the Υ_* value compared to that which we determine from the SPS fits presented in Section 3. Using the constraint we derive from SPS, we add an additional χ^2 term containing $\Delta\Upsilon_{*,R} = 0.8$ with a central value of $\Upsilon_{*,R} = 1.1$ to the χ^2 values from the kinematics per

$$\chi^2 = \left(\frac{\Upsilon_* - \hat{\Upsilon}_*}{\Delta\Upsilon_*}\right)^2 + \sum_{i=1}^{N_{\mathrm{bins}}} \left(\frac{v_{i,\mathrm{rms}} - v_{i,\mathrm{model}}}{\Delta v_{i,\mathrm{rms}}}\right)^2. \quad (3)$$

The parameters then reach a minimum at $\Upsilon_{*,R} = 1.158$, $i = 65.^\circ0$, $\beta_z = 0.450$, $\rho_0(r = 1\,\mathrm{pc}) = 45.7\,M_\odot\ \mathrm{pc}^{-3}$, and $\alpha = 0.90$ at $\chi^2_{\nu=88} = 77.1$. By marginalizing over the other four parameters, the data disfavor $\alpha = 1$ at 0.8σ significance, $\alpha = 0.6$ at 1σ significance, and $\alpha = 0$ at 2.2σ significance. The V_{rms} map and residuals are shown in Figure 11. The enclosed mass model is shown for the joint constraint in Figure 12. This solution is within the 1σ confidence interval from the kinematic data only. Finally, we fix $\Upsilon_{*,R} = 1$ and $\alpha = 0.1$ as an illustration of a cored DM model. The V_{rms} map and residuals are shown in Figure 11. After optimizing the remaining three variables, this model yields $\chi^2_{\nu=88} = 93.9$ and is excluded with high confidence. The crucial difference between this final model and the data is in the generally more circular V_{rms} contour in the former.

[7] http://cow.physics.wisc.edu/~craigm/idl/idl.html

4.4. Parameter Degeneracies

We here investigate the degeneracy between α and Υ_*. By our parameterization, there is an obvious degeneracy between ρ_0 and α with a weaker degeneracy on Υ_* (Figure 13). The most important degeneracy for the purpose of constraining the mass budget is that between Υ_* and α. In NGC 2976, they anti-correlate. A similar exercise is done with the joint kinematic and SPS likelihoods by which the cored DM fit is excluded at 2σ significance, but a pure cusp is permitted. We conclude that honoring even a loose Υ_* limit makes a DM halo measurement entirely consistent with the NFW form. The cored model is disfavored at modest significance but amenable to stricter limits through more extended instrument pointings and higher S/N data.

4.5. Other DM Distributions

We apply the power-law function as the primary DM density distribution, but we briefly test and discuss alternatives. The pseudo-isothermal function is commonly applied to DM halo data as a well-fitting cored model, although it lacks theoretical motivation. The pseudo-isothermal function

$$\rho(r) = \frac{\rho_0}{1+(r/r_c)^2} \quad (4)$$

contains a central DM space density of ρ_0 and scale length of r_c. In the limit of r_c significantly larger than the data points, a power-law function with $\alpha = 0$ mimics this function. However, the added flexibility of the scale length term can diminish the capability to discriminate between cores and cusps. The best-fit, five-parameter model with the SPS penalty has a minimum at $\Upsilon_{*,R} = 1.37$, $i = 66.^\circ4$, $\beta_z = 0.390$, $\rho_0 = 0.198\,M_\odot\ \mathrm{pc}^{-3}$, and $r_c = 1.0$ kpc at $\chi^2_{\nu=88} = 78.3$. The steep, power-law model is still preferred, but the cored model is statistically viable. Data at larger radii are necessary to better test for the presence of a large core.

Next, we test a six-parameter model with the NFW form. A minimization of the full NFW function requires a large-scale radius, r_s, for a quality fit. Only models with $r_s > 10$ kpc fit well where the power-law approximation becomes highly precise. This results in an enormous DM virial mass ($\sim 2 \times 10^{11}\,M_\odot$), but data at larger radii are necessary to make a reliable estimate of the virial mass.

5. MODELS FROM GAS KINEMATICS

The [O II] data are fit with a TR (Rogstad et al. 1974, 1976) and harmonic decomposition (HD) algorithm to determine a rotation curve assuming an infinitely thin geometry for the gas. The code is the same as used and described in Fathi et al. (2005). The HD model and terms are shown in Figure 14 as is the TR model. Driven by the same complex structures and kinematic twists as discussed by SBLB03 for the Hα in this galaxy, we have made harmonic fits through the $m = 3$ terms. SBLB03 only present circular and radial terms, however. Our TR fit is allowed a position angle that varies with radius, which can also explain the kinematic twist. The [O II] rotation curves are given in Table 3 and shown in Figure 15. The asymmetric drift correction for the ionized gas in NGC 2976 has been calculated in SBLB03, found to be small, and not used in their analysis because of substantial uncertainties in its exact value. Similarly, we do not apply an asymmetric drift correction to our gas rotation curve fits. There is consistency between the shapes of our [O II] rotation curve

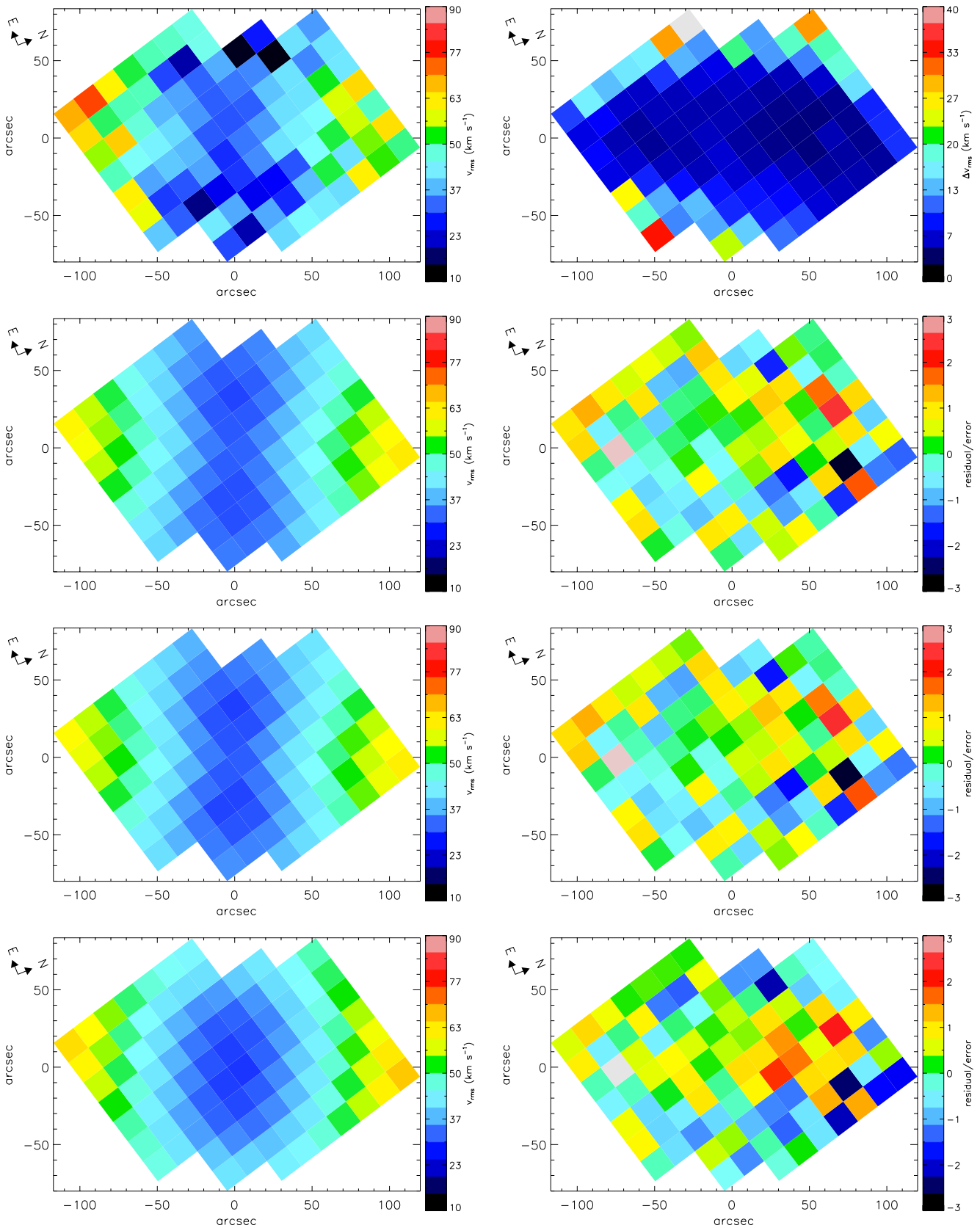

Figure 11. Left: $V_{\rm rms}$. Right: $V_{\rm rms}$ error for the data and residual/error for the models. Row 1: data. Row 2: the model at the least-squares minimum fit made to the kinematic data alone. This model disagrees with the SPS determination on $\Upsilon_{*,R}$. The model is characterized by $\chi^2_{\nu=87} = 77.0$. Row 3: the model at the least-squares minimum fit to the combined SPS and kinematic data. Including the SPS penalty, the fit is characterized by $\chi^2_{\nu=88} = 77.1$. Row 4: the model second-moment velocity map for a fit fixed to $\Upsilon_{*,R} = 1.1$, $\alpha = 0.1$, and the remaining parameters freely fit. This model represents the class of DM dominated and cored models that are excluded by our data. The penalty in χ^2 comes from model velocities that rise more slowly than the data along the major axis and excess model velocities at minor axis offsets. This fit is characterized by $\chi^2_{\nu=89} = 93.9$.

(A color version of this figure is available in the online journal.)

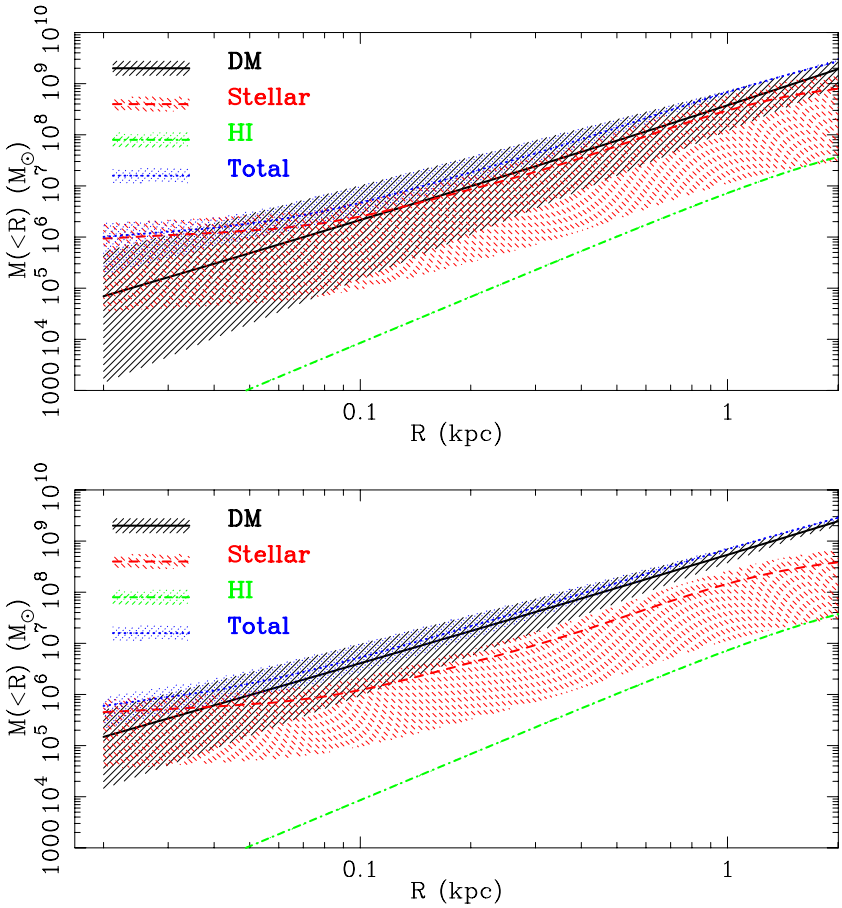

Figure 12. Enclosed mass profiles and confidence intervals. Top: using the kinematic data alone. The $\Upsilon_{*,R}$ fit here exceeds that fit through stellar population synthesis analysis. With these poor constraints, NGC 2976 may be DM or baryon dominated to the largest radius measured. The median models have similar amounts of enclosed DM and stellar mass up to 1 kpc where the DM begins to dominate. Bottom: using the combined SPS and kinematic data. The DM halo dominates at least to $r > 200$ pc and perhaps everywhere.

(A color version of this figure is available in the online journal.)

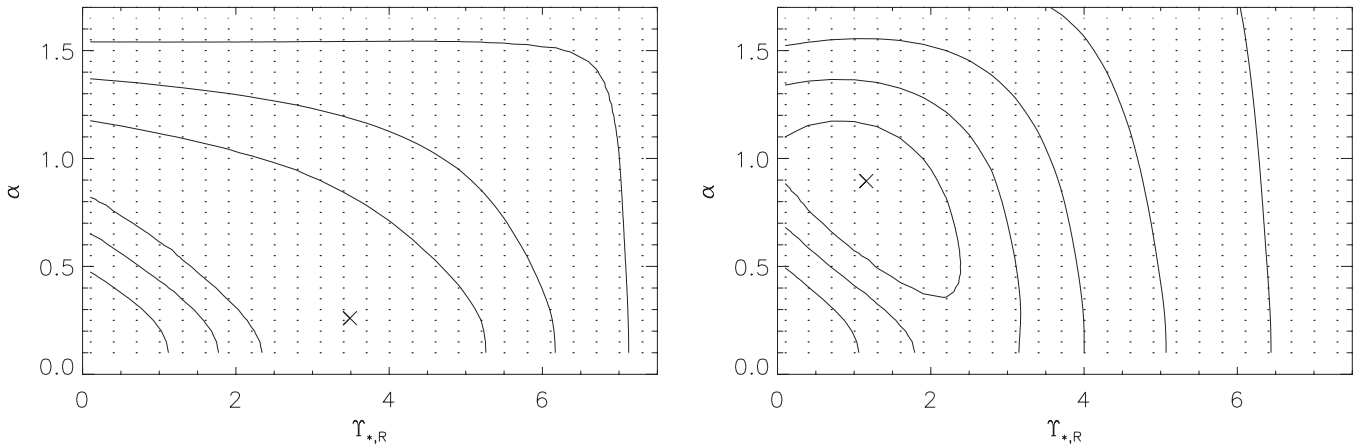

Figure 13. $\Delta\chi^2$ distributions for combinations of the five parameters being minimized in the Jeans modeling. The inner three contours correspond to $\Delta\chi^2 = 2.3$, 6.2, and 12.9 or 1σ, 2σ, and 3σ significance. The additional contours increase each by a factor of two. Cross symbols mark the formal minima. Left: the confidence intervals from the kinematic data alone. Right: the confidence intervals when the kinematic and SPS data are combined.

and the Hα rotation curve of SBLB03. The irregular structure in the curve at $r = 30''$ and $r = 60''$ is found in both data sets, particularly in our TR fit.

We next fit a velocity power law of the form $v_{\rm circ,DM} \propto r^{\beta}$ added in quadrature to the stellar and H I component circular velocities. The circular velocity of a power-law density profile is a power law with a different index. The well-known relation for the density and circular velocity indices for power laws of $\alpha = 2 \times (1 - \beta)$ (e.g., SBLB03, Appendix B) is used. A variety of Υ_* values are tested as detailed in Table 5, some fixed and some fit live. We also refit the SBLB03 data of their Table 3 in the same manner, taking their mass model rotation curves and trying their maximal disk value of $\Upsilon_{*,K} = 0.19$. The residuals from the best fit were used to estimate the uncertainty in the

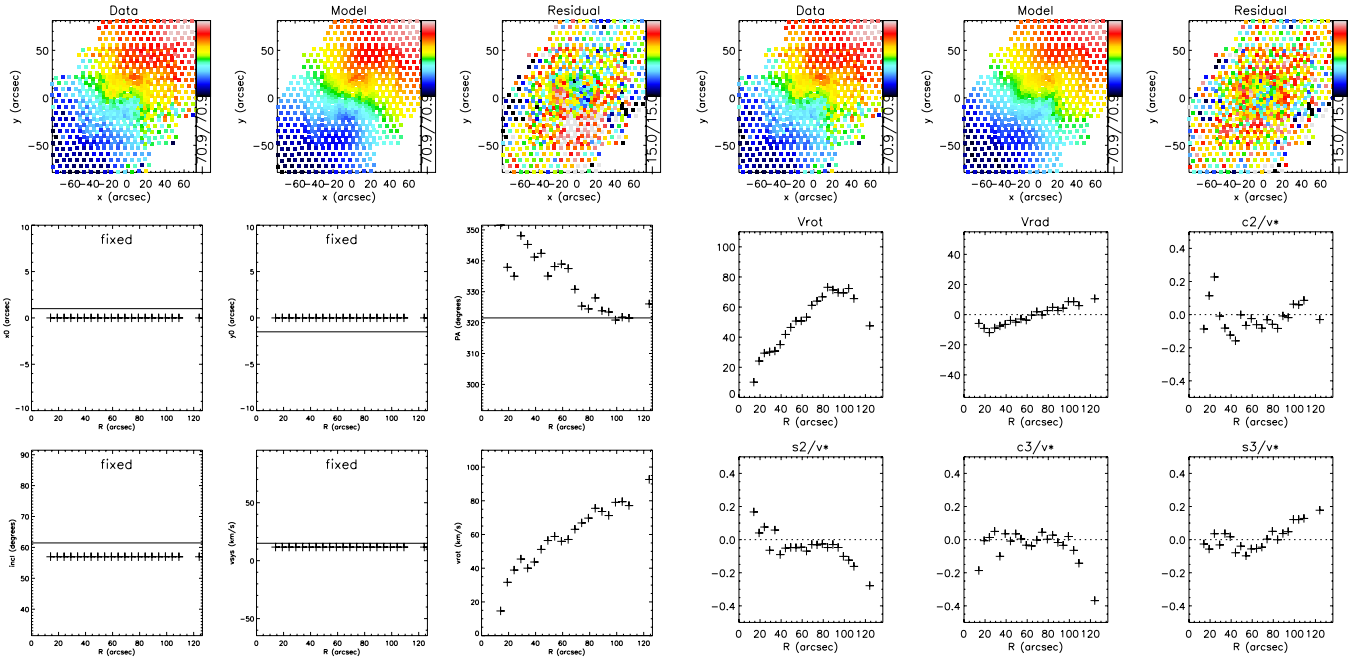

Figure 14. Data and fits to the [O II] velocity field representing the two ways that the kinematic twist can be recovered. Left: the fit with a tilted-ring (TR) model and a variable position angle. Right: the fit with a harmonic decomposition (HD) model through three orders. Significant radial velocity is observed, particularly in the galaxy's center. The sign of the radial velocity is uncertainty as we cannot identify the galaxy's near side. If we speculate that the galaxy's near side is in the SW, the gas near the center is outflowing. The higher-order terms are noisy, but similar rotational and radial velocity fits are made when the higher-order terms are not fit.
(A color version of this figure is available in the online journal.)

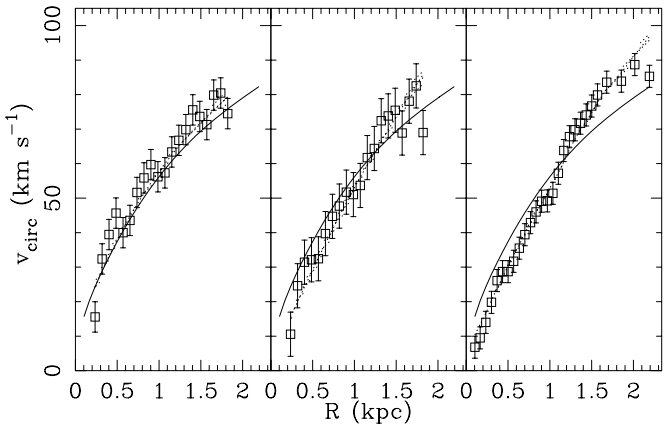

Figure 15. Comparison between the circular velocity determinations from stellar and gas kinematics. The solid line in each panel shows the circular velocity for the mass model favored by the stellar kinematics with an SPS penalty (right panel of Figure 13). The circular velocity as determined by the gas kinematics is shown with data points and the dotted line as a power-law fit. The 68% confidence interval is indicated by an upper and lower dotted line. The fits to the gas data use fixed Υ_* values per Table 5. Left: the [O II] data and fit for the tilted-ring model with a varying position angle. Middle: the [O II] data and fit for the harmonic decomposition model through third order. The fit is steeper than the stellar-based model and consistent with a cored DM halo. Right: the Hα data of SBLB03. These data are fit by removing a radial velocity component at small radius and similar to our [O II] harmonic decomposition model.

Table 5
Dark Matter Density Index Constraints from Gaseous Kinematics[a]

Assumption	This Data Set's Tilted Ring Fit	This Data Set's Harmonic Decomposition	SBLB03 Data Set
$\Upsilon_* = 0$	0.80 ± 0.08	0.31 ± 0.13	0.43 ± 0.06
Υ_* fixed[b]	0.84 ± 0.10	0.14 ± 0.17	0.16 ± 0.08
Freely fit Υ_*	0.81 ± 2.20	0.31 ± 0.98	0.12 ± 0.44

Notes.
[a] The confidence ranges are based on rms circular velocity uncertainties in order to capture both statistical and systematic errors.
[b] Assuming $\Upsilon_{*,R} = 1.1$ for our data and $\Upsilon_{*,K} = 0.19$ for the SBLB03 data.

rotation curve; these systematic uncertainties are larger than the statistical errors and included in the error determination of α.

The estimates of α from the gas kinematics are presented in Table 5 for a variety of data sets and assumptions on Υ_*. The HD fits to the [O II] data require a cored DM halo, regardless of the Υ_* assumptions. The [O II] TR fits require DM slopes that are steeper than the HD fits at 3σ significance, but still deviating from NFW expectations at 1.5σ significance. The HD can fit for radial infall or outflow, but some other motions may be degenerate with rotation such as the motions due to a bar-like potential (Spekkens & Sellwood 2007). A bar is expected to show power in the third-order terms, and our $m = 3$ sine term does show some power at large radius. Finally, we fit the HD data of SBLB03 in the same manner. From their fits with a range in Υ_* chosen to represent maximal and submaximal disks, SBLB03 reach ranges of $0.01 < \alpha < 0.17$. We find agreement with their determinations. We find a larger, but still deviating from a cusp by 5σ significance, DM halo slope when we constrain the disk to have no mass. We conclude that a mass model based on the gas data with a single position angle and harmonic terms favors a cored DM halo, but that this result is not robust against an equally viable model that fits the data with a twist in the position angle. The mass profile conclusions drawn from the gas kinematics in this object are subject to severe dependencies in the modeling choices.

A comparison between the gas velocity field in Figure 14 and the stellar line-of-sight velocity in Figure 6 shows that the zero velocity contours in both are twisted in the same way and with similar magnitude along the minor axis. This may

be an important clue to the cause of the non-regular motions as collisional processes are expected to not twist the stellar zero velocity contour. One explanation may be that both the stars and gas have their angular momentum vectors perturbed at small radius, perhaps by bending in a weak bar potential. In this case, the stellar models are more immune to a warp as the Jeans models compare to $V_{\rm rms}$ instead of simply $V_{\rm los}$, and we measure a stellar velocity dispersion that is larger than line-of-sight rotation out to $R_{\rm maj} \sim 60''$. With the current level of stellar, observational errors, the axisymmetric models we present are statistically sufficient to describe the galaxy. Better data, taken in the future, may merit analysis with non-axisymmetric orbit-based models.

6. CONCLUSIONS

We present two-dimensional maps of stellar and gaseous kinematics in the late-type dwarf galaxy NGC 2976. Theoretical models of collisionless, cold DM predict a cuspy DM halo to exist in low mass halos when gravity alone is simulated. Baryonic feedback processes have been proposed as a mechanism to create a cored halo, which observations such as ours may constrain. The leverage of the stellar kinematics as a collisionless tracer is a major advantage to our work. We fit the stellar kinematics with an axisymmetric, semi-isotropic Jeans model to measure the DM profile and constrain Υ_*. The Jeans model permits both a cored or cuspy halo with a mild preference for a cored, high $\Upsilon_{*,R}$. We next fit a suite of stellar population histories to an optical spectrum with a broader bandpass. We find a limit of $\Upsilon_{*,R} = 1.1 \pm 0.8$ driven primarily by uncertainty in the IMF. This limit in combination with the kinematic data provides a much tighter certainty on the DM profile. The combined fit suggests a DM cusp ($\alpha = 0.90 \pm 0.15$ at 1σ) and excludes a DM core at 2σ significance. NGC 2976 is DM dominated everywhere outside of the nuclear star cluster and requires no history of baryonic feedback or non-standard particle properties to explain the DM halo profile. The gaseous kinematics, in concordance with earlier work, imply a cored DM halo when modeled with an HD method and a single position angle. A TR fit with a variable position angle instead excludes the cored model and is compatible with the models fit by the stellar kinematics. A larger sample with stellar kinematics is needed to compare with the vast literature on gaseous kinematics and reassess the quantity and distribution of DM and possible correlations with central density slope in late-type dwarf galaxies. This work comes with two primary caveats that can be improved upon. First, our results are strongest for a DM density power-law approximation, and a DM density model with a large core under a different parameterization cannot be strictly excluded with the current data as discussed in Section 4.5. Data at larger radii, such as >2 kpc, will close this uncertainty but require a deeper flux limit. Second, a crucial barrier to achieving lower statistical errors in this work has been the large instrumental resolution relative to the intrinsic dispersion. In future works, we will use the newly available Visible Integral Field Replicable Unit Spectrograph Wendelstein (Fabricius et al. 2008) at a resolution of $R = 6800$ to circumvent this limitation.

J.J.A. acknowledges a National Science Foundation Graduate Student Fellowship and a UT Harrington Endowment Dissertation Fellowship that have supported him through this work. K.G. acknowledges support from NSF-0908639. We are grateful to Josh Simon for providing important suggestions during this paper's editing. We thank George and Cynthia Mitchell for funding the VIRUS-P instrument. This research has made use of the NASA/IPAC Extragalactic Database (NED) which is operated by the Jet Propulsion Laboratory, California Institute of Technology, under contract with the National Aeronautics and Space Administration. We have used MGE and JAM as written and distributed by Michele Cappellari; we thank him for his fine work. This work made use of THINGS, "The H I Nearby Galaxy Survey," and SINGS, the "Spitzer Infrared Nearby Galaxies Survey"; we thank them for their public data release. We note that the public availability of the Simon et al. (2003) CO data and tabular rotation curves were used here for comparison and appreciated. Finally, we thank an anonymous referee for important improvements to this work.

Facility: Smith (VIRUS-P)

REFERENCES

Adams, J. J., Blanc, G. A., Hill, G. J., et al. 2011, ApJS, 192, 5
Alongi, M., Bertelli, G., Bressan, A., et al. 1993, A&AS, 97, 851
Bahcall, J. N., & Casertano, S. 1984, ApJ, 284, L35
Bell, E. F., & de Jong, R. S. 2001, ApJ, 550, 212
Bershady, M. A., Martinsson, T. P. K., Verheijen, M. A. W., et al. 2011, ApJ, 739, L47
Bershady, M. A., Verheijen, M. A. W., Swaters, R. A., et al. 2010a, ApJ, 716, 198
Bershady, M. A., Verheijen, M. A. W., Westfall, K. B., et al. 2010b, ApJ, 716, 234
Binney, J., & Merrifield, M. (ed.) 1998, Galactic Astronomy (Princeton, NJ: Princeton Univ. Press)
Bottema, R. 1989a, A&A, 225, 358
Bottema, R. 1989b, A&A, 221, 236
Bottema, R. 1990, A&A, 233, 372
Bottema, R. 1992, A&A, 257, 69
Bottema, R., van der Kruit, P. C., & Freeman, K. C. 1987, A&A, 178, 77
Bottema, R., van der Kruit, P. C., & Valentijn, E. A. 1991, A&A, 247, 357
Brammer, G. B., van Dokkum, P. G., & Coppi, P. 2008, ApJ, 686, 1503
Bressan, A., Fagotto, F., Bertelli, G., & Chiosi, C. 1993, A&AS, 100, 647
Bruzual, G. 2007, arXiv:astro-ph/0703052
Bruzual, G., & Charlot, S. 2003, MNRAS, 344, 1000
Calzetti, D., Armus, L., Bohlin, R. C., et al. 2000, ApJ, 533, 682
Cappellari, M. 2002, MNRAS, 333, 400
Cappellari, M. 2008, MNRAS, 390, 71
Cappellari, M., Bacon, R., Bureau, M., et al. 2006, MNRAS, 366, 1126
Cappellari, M., Emsellem, E., Bacon, R., et al. 2007, MNRAS, 379, 418
Copin, Y., Cretton, N., & Emsellem, E. 2004, A&A, 415, 889
Corbelli, E., & Walterbos, R. A. M. 2007, ApJ, 669, 315
Corsini, E. M., Pizzella, A., Sarzi, M., et al. 1999, A&A, 342, 671
Dalcanton, J. J., Williams, B. F., Seth, A. C., et al. 2009, ApJS, 183, 67
Dale, D. A., Gil de Paz, A., Gordon, K. D., et al. 2007, ApJ, 655, 863
de Blok, W. J. G., Walter, F., Brinks, E., et al. 2008, AJ, 136, 2648
de Vaucouleurs, G., de Vaucouleurs, A., Corwin, H. G., Jr., et al. (ed.) 1991, Third Reference Catalogue of Bright Galaxies (New York: Springer)
Diemand, J., Kuhlen, M., Madau, P., et al. 2008, Nature, 454, 735
Emsellem, E., Monnet, G., & Bacon, R. 1994, A&A, 285, 723
Fabricius, M. H., Barnes, S., Bender, R., et al. 2008, Proc. SPIE, 7014, 234
Fagotto, F., Bressan, A., Bertelli, G., & Chiosi, C. 1994a, A&AS, 104, 365
Fagotto, F., Bressan, A., Bertelli, G., & Chiosi, C. 1994b, A&AS, 105, 29
Fathi, K., van de Ven, G., Peletier, R. F., et al. 2005, MNRAS, 364, 773
Gebhardt, K., Richstone, D., Kormendy, J., et al. 2000, AJ, 119, 1157
Girardi, L., Bressan, A., Chiosi, C., Bertelli, G., & Nasi, E. 1996, A&AS, 117, 113
Goodman, J. 2000, New Astron., 5, 103
Governato, F., Brook, C., Mayer, L., et al. 2010, Nature, 463, 203
Herrmann, K. A., & Ciardullo, R. 2009, ApJ, 705, 1686
Hill, G. J., MacQueen, P. J., Palunas, P., Barnes, S. I., & Shetrone, M. D. 2008, Proc. SPIE, 7014, 231
Ho, L. C., Greene, J. E., Filippenko, A. V., & Sargent, W. L. W. 2009, ApJS, 183, 1
Hogan, C. J., & Dalcanton, J. J. 2000, Phys. Rev. D, 62, 063511
Karachentsev, I. D., Dolphin, A. E., Geisler, D., et al. 2002, A&A, 383, 125
Kauffmann, G., Heckman, T. M., White, S. D. M., et al. 2003, MNRAS, 341, 33
Kennicutt, R. C., Jr., Armus, L., Bendo, G., et al. 2003, PASP, 115, 928

Krajnović, D., Cappellari, M., Emsellem, E., McDermid, R. M., & de Zeeuw, P. T. 2005, MNRAS, 357, 1113
Kurucz, R. L., Furenlid, I., Brault, J., & Testerman, L. 1984, Solar Flux Atlas from 296 to 1300 nm (New Mexico: National Solar Observatory)
Kuzio de Naray, R., McGaugh, S. S., & de Blok, W. J. G. 2008, ApJ, 676, 920
Maraston, C. 2005, MNRAS, 362, 799
Marigo, P., & Girardi, L. 2007, A&A, 469, 239
Menéndez-Delmestre, K., Sheth, K., Schinnerer, E., Jarrett, T. H., & Scoville, N. Z. 2007, ApJ, 657, 790
Murphy, J. D., Gebhardt, K., & Adams, J. J. 2011, ApJ, 729, 129
Navarro, J. F., Eke, V. R., & Frenk, C. S. 1996a, MNRAS, 283, L72
Navarro, J. F., Frenk, C. S., & White, S. D. M. 1996b, ApJ, 462, 563
Oh, S., de Blok, W. J. G., Brinks, E., Walter, F., & Kennicutt, R. C., Jr. 2011, AJ, 141, 193
Oh, S., de Blok, W. J. G., Walter, F., Brinks, E., & Kennicutt, R. C. 2008, AJ, 136, 2761
Peebles, P. J. E. 2000, ApJ, 534, L127
Portinari, L., Sommer-Larsen, J., & Tantalo, R. 2004, MNRAS, 347, 691
Prescott, M. K. M., Kennicutt, R. C., Jr., Bendo, G. J., et al. 2007, ApJ, 668, 182
Prugniel, P., & Soubiran, C. 2001, A&A, 369, 1048
Rhee, G., Valenzuela, O., Klypin, A., Holtzman, J., & Moorthy, B. 2004, ApJ, 617, 1059
Rindler-Daller, T., & Shapiro, P. R. 2011, arXiv:1106.1256
Rogstad, D. H., Lockhart, I. A., & Wright, M. C. H. 1974, ApJ, 193, 309
Rogstad, D. H., Wright, M. C. H., & Lockhart, I. A. 1976, ApJ, 204, 703
Sakai, S., Mould, J. R., Hughes, S. M. G., et al. 2000, ApJ, 529, 698
Schwarzschild, M. 1979, ApJ, 232, 236
Shapiro, K. L., Gerssen, J., & van der Marel, R. P. 2003, AJ, 126, 2707
Simon, J. D., Bolatto, A. D., Leroy, A., & Blitz, L. 2003, ApJ, 596, 957
Simon, J. D., Bolatto, A. D., Leroy, A., Blitz, L., & Gates, E. L. 2005, ApJ, 621, 757
Spano, M., Marcelin, M., Amram, P., et al. 2008, MNRAS, 383, 297
Spekkens, K., & Sellwood, J. A. 2007, ApJ, 664, 204
Spergel, D. N., & Steinhardt, P. J. 2000, Phys. Rev. Lett., 84, 3760
Stil, J. M., & Israel, F. P. 2002a, A&A, 389, 29
Stil, J. M., & Israel, F. P. 2002b, A&A, 389, 42
Swaters, R. A. 1999, PhD thesis, Rijksuniversiteit Groningen
Swaters, R. A., Madore, B. F., van den Bosch, F. C., & Balcells, M. 2003, ApJ, 583, 732
Thomas, J., Jesseit, R., Saglia, R. P., et al. 2009, MNRAS, 393, 641
Tremonti, C. A., Heckman, T. M., Kauffmann, G., et al. 2004, ApJ, 613, 898
Valenzuela, O., Rhee, G., Klypin, A., et al. 2007, ApJ, 657, 773
van den Bosch, R. C. E., van de Ven, G., Verolme, E. K., Cappellari, M., & de Zeeuw, P. T. 2008, MNRAS, 385, 647
van der Kruit, P. C., & de Grijs, R. 1999, A&A, 352, 129
van der Kruit, P. C., & Freeman, K. C. 1984, ApJ, 278, 81
van der Kruit, P. C., & Freeman, K. C. 1986, ApJ, 303, 556
Walter, F., Brinks, E., de Blok, W. J. G., et al. 2008, AJ, 136, 2563
Weijmans, A.-M., Cappellari, M., Bacon, R., et al. 2009, MNRAS, 398, 561
Weinberg, M. D., & Katz, N. 2002, ApJ, 580, 627
Williams, B. F., Dalcanton, J. J., Stilp, A., et al. 2010, ApJ, 709, 135
Worthey, G., Faber, S. M., Gonzalez, J. J., & Burstein, D. 1994, ApJS, 94, 687
Zibetti, S., Charlot, S., & Rix, H.-W. 2009, MNRAS, 400, 1181